NASA / TM—1998-107249 / CH4

Solid Lubrication Fundamentals and Applications

Properties of Contaminated Surfaces: Adhesion, Friction, and Wear

Kazuhisa Miyoshi
Lewis Research Center, Cleveland, Ohio

July 1998

The NASA STI Program Office . . . in Profile

Since its founding, NASA has been dedicated to the advancement of aeronautics and space science. The NASA Scientific and Technical Information (STI) Program Office plays a key part in helping NASA maintain this important role.

The NASA STI Program Office is operated by Langley Research Center, the Lead Center for NASA's scientific and technical information. The NASA STI Program Office provides access to the NASA STI Database, the largest collection of aeronautical and space science STI in the world. The Program Office is also NASA's institutional mechanism for disseminating the results of its research and development activities. These results are published by NASA in the NASA STI Report Series, which includes the following report types:

- TECHNICAL PUBLICATION. Reports of completed research or a major significant phase of research that present the results of NASA programs and include extensive data or theoretical analysis. Includes compilations of significant scientific and technical data and information deemed to be of continuing reference value. NASA's counterpart of peer-reviewed formal professional papers but has less stringent limitations on manuscript length and extent of graphic presentations.

- TECHNICAL MEMORANDUM. Scientific and technical findings that are preliminary or of specialized interest, e.g., quick release reports, working papers, and bibliographies that contain minimal annotation. Does not contain extensive analysis.

- CONTRACTOR REPORT. Scientific and technical findings by NASA-sponsored contractors and grantees.

- CONFERENCE PUBLICATION. Collected papers from scientific and technical conferences, symposia, seminars, or other meetings sponsored or cosponsored by NASA.

- SPECIAL PUBLICATION. Scientific, technical, or historical information from NASA programs, projects, and missions, often concerned with subjects having substantial public interest.

- TECHNICAL TRANSLATION. English-language translations of foreign scientific and technical material pertinent to NASA's mission.

Specialized services that complement the STI Program Office's diverse offerings include creating custom thesauri, building customized data bases, organizing and publishing research results . . . even providing videos.

For more information about the NASA STI Program Office, see the following:

- Access the NASA STI Program Home Page at *http://www.sti.nasa.gov*

- E-mail your question via the Internet to help@sti.nasa.gov

- Fax your question to the NASA Access Help Desk at (301) 621-0134

- Telephone the NASA Access Help Desk at (301) 621-0390

- Write to:
  NASA Access Help Desk
  NASA Center for AeroSpace Information
  800 Elkridge Landing Road
  Linthicum Heights, MD 21090-2934

NASA / TM—1998-107249 / CH4

Solid Lubrication Fundamentals and Applications

Properties of Contaminated Surfaces: Adhesion, Friction, and Wear

Kazuhisa Miyoshi
Lewis Research Center, Cleveland, Ohio

National Aeronautics and
Space Administration

Lewis Research Center

July 1998

Available from

NASA Center for Aerospace Information
800 Elkridge Landing Road
Linthicum Heights, MD 21090-2934
Price Code: A05

National Technical Information Service
5287 Port Royal Road
Springfield, VA 22100
Price Code: A05

Chapter 4
Properties of Contaminated Surfaces: Adhesion, Friction, and Wear

4.1 Introduction

When atomically clean, unlubricated surfaces are brought together under a normal load, the atoms at the surfaces must, at some points, be in contact. Then, the basic material properties of the solids themselves become extremely important in the adhesion, friction, and wear behavior of the materials, as described in Chapter 3. In most practical situations, however, contaminant layers, such as carbon compounds and water, are ubiquitous and are present on any solid surface that has been exposed to air. Even a supposedly "clean" material surface will show a significant carbon, oxygen, and water contribution to the Auger electron spectroscopy (AES) and x-ray photoelectron spectroscopy (XPS) spectrum because one or more layers of adsorbed hydrocarbons and oxides of carbon are present [4.1–4.4]. These contaminant layers mask the surface features of the solids in tribological contact. For example, a major characteristic of material wear is that for unlubricated surfaces the wear rate covers an enormous range (say 10^{-2} to 10^{-10} mm^3/N-m) while the coefficient of friction varies relatively little (0.01 to 1.5 in air). The small coefficient-of-friction range occurs because the solid surfaces in dry contact are masked by the contaminant layers. The friction between unlubricated surfaces is due to shearing in the adsorbed contaminant films, although these films may be partially destroyed by the sliding process.

This chapter presents the fundamental tribology of contaminated surfaces (i.e., the adhesion, friction, and wear behavior of smooth but contaminated surfaces of solid-solid couples, such as metal-ceramic couples). The subjects to be addressed include the effects of (1) surface contamination by the interaction of a surface with the environment, (2) surface contamination by diffusion of bulk elements or compounds, and (3) surface chemical changes with selective thermal evaporation [4.3, 4.4].

4.2 Effects of Surface Contamination by Environment

4.2.1 Ubiquitous Contamination From Atmosphere

Nonoxide ceramics.—Pull-off forces (adhesion) and coefficients of friction for hot-pressed polycrystalline silicon nitride (Si_3N_4) in contact with metals were examined in an ultra-high-vacuum environment [4.3, 4.4] by using the method described in Chapter 3.

Figure 4.1 shows the marked difference in adhesion for two surface conditions, contaminated (as received) surfaces and sputter-cleaned surfaces, in ultrahigh vacuum. Chemical interactions normally play an important role in the adhesion of silicon nitride–metal couples. With contaminated surfaces, however, the chemical activity or inactivity of the metal did not appear to play a role in adhesion (Fig. 4.1). Adhesion for the various as-received metals in contact with Si_3N_4 generally remained constant. In contrast, the adhesion properties for the sputter-cleaned surfaces were related to the relative chemical activity (percentage of d valence bond character) of the transition metals as a group, and adhesion was higher than for the as-received surfaces. According to Pauling's theory [4.5] the greater the percentage of d valence bond character, the less active the metal and the lower the pull-off force required to break the bonds. Thus, the adhesion results (Fig. 4.1) show that the more active the metal, the higher the adhesion. This conclusion is consistent with the

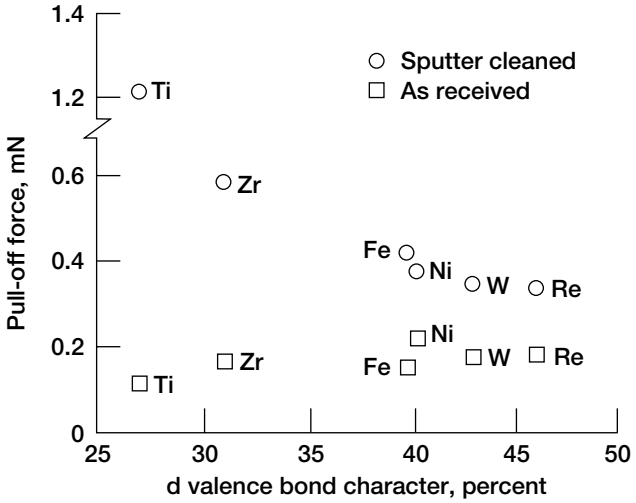

Figure 4.1.—Pull-off force (adhesion) as function of percentage of d valence bond character for transition metals in contact with monolithic Si_3N_4 in vacuum. From [4.5].

friction studies conducted on the surfaces of other nonmetal-metal couples (see Chapter 3). But why does this appreciable difference in adhesion occur for the two surface conditions, contaminated and sputter cleaned? Analyzing the surface chemistry of the foregoing Si_3N_4 specimens will assist us in understanding adhesion behavior.

XPS survey spectra of an as-received Si_3N_4 surface (Fig. 4.2(a)) reveal an adsorbed carbon peak as well as an oxygen peak. An adsorbate layer on the surface consisted of hydrocarbons and water vapor that may have condensed from the environment and become physically adsorbed to the Si_3N_4 surface. The contamination layer could be removed by ion etching just before analysis. But, since the ion beam itself can induce compositional changes in the specimen surface, it had to be used with care. After the Si_3N_4 surface was cleaned by argon ion sputtering, the carbon and oxygen contamination peaks became very small (Fig. 4.2(b)), and the peak intensity of both the silicon and nitrogen associated with Si_3N_4 increased markedly. The small amount of carbon and oxygen was associated with bulk contaminants of the Si_3N_4.

Comparing Fig. 4.1 with Fig. 4.2 shows that a prerequisite for the sameness in adhesion of as-received surfaces of ceramic-metal couples is that the surfaces be covered with a stable layer of contaminants. Thus, contaminant films on the surfaces of ceramics and metals can greatly reduce adhesion.

Friction results for boron nitride (BN) coatings in contact with metals in ultrahigh vacuum (Fig. 4.3) are analogous to the adhesion results (Fig. 4.1). The similar shapes of Figs. 4.1 and 4.3 are not surprising because XPS survey spectra of the as-received BN film surface reveal a carbon contaminant peak as well as an adsorbed

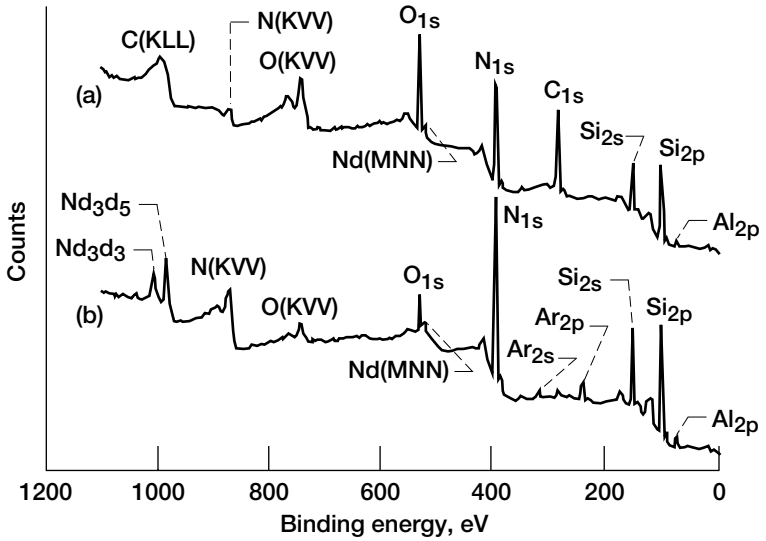

Figure 4.2.—XPS spectra of Si_3N_4 before (a) and after (b) ion sputtering.

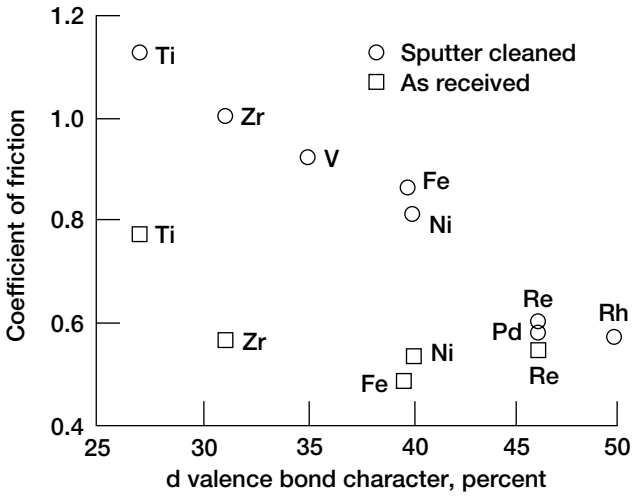

Figure 4.3.—Coefficient of friction as function of d valence bond character of metals in sliding contact with ion-beam-deposited BN film in ultrahigh vacuum.

oxygen peak [4.6]. The friction results, as shown in Fig. 4.3, indicate that for the sputter-cleaned surfaces the coefficients of friction were low at higher percentages of d valence bond character but were generally the same at all percentages for the as-received surfaces. Only the as-received surfaces of the BN-titanium couple showed a somewhat higher coefficient of friction, perhaps because the contaminant films adsorbed on these surfaces were partially destroyed during sliding. An adsorbate layer on the surface consisted of water vapor and hydrocarbons that may have condensed from the environment and become physically adsorbed to the BN film. After the BN film surfaces had been sputter cleaned with argon ions, although there were still small carbon and oxygen contamination peaks, the boron and nitrogen peaks predominated (Fig. 4.4).

The boron nitride B_{1s} photoelectron emission lines (Fig. 4.4) peaked primarily at 190 eV, which is associated with BN. They also included a small amount of boron carbide (B_4C). The N_{1s} photoelectron emission lines peaked primarily at 397.9 eV, which again is associated with BN. The C_{1s} photoelectron lines taken from the as-received surface at 284.6 eV indicate the presence of adventitious adsorbed carbon contamination with a small amount of carbide. After sputter cleaning the adsorbed carbon contamination peak disappeared from the spectrum, and the relatively small carbide peak could be seen. The O_{1s} photoelectron lines of the as-received BN surface peaked at 531.6 eV because of adsorbed oxygen contamination and oxides. After argon sputter cleaning the adsorbed oxygen contamination peak disappeared from the spectrum, but the small oxide peak remained. Thus, the peak intensities for both boron and nitrogen associated with BN increased with argon ion sputter cleaning, but those for carbon and oxygen decreased markedly.

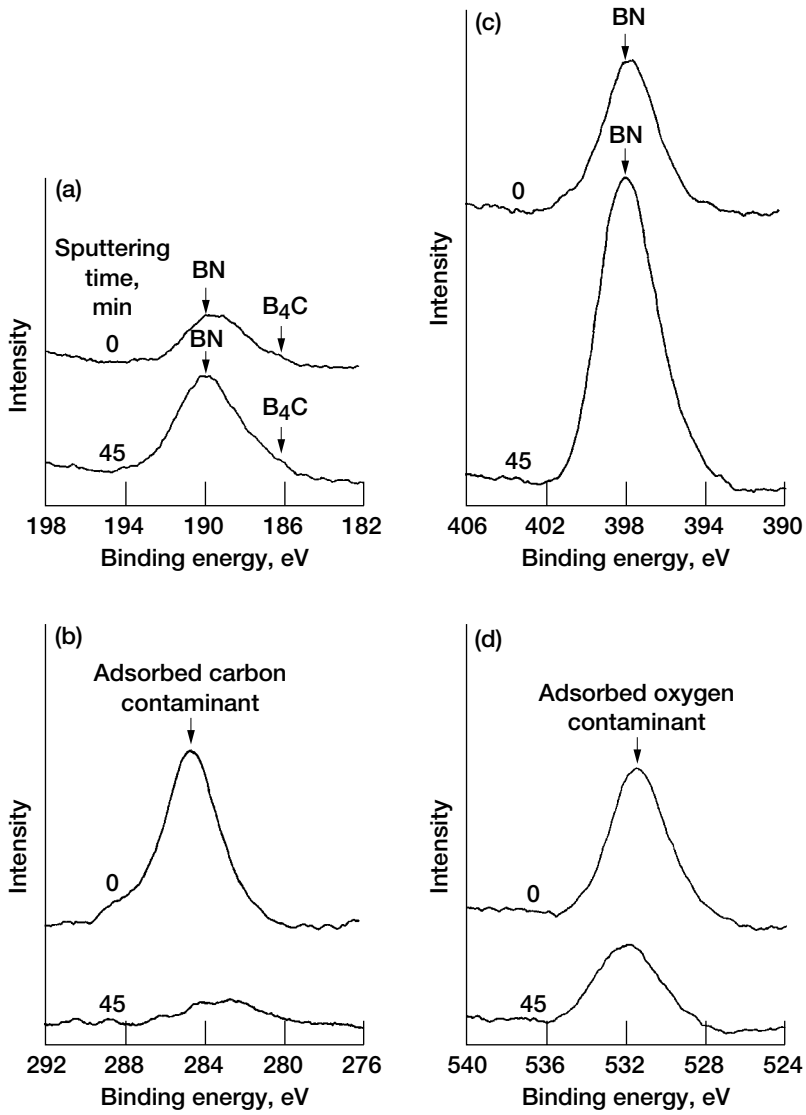

Figure 4.4.—XPS peaks of BN films deposited on 440C stainless steel. Pass energy, 25 eV; energy resolution, 0.5 eV. (a) B_{1s}. (b) N_{1s}. (c) C_{1s}. (d) O_{1s}.

The BN film deposited on a 440C stainless steel substrate was nonstoichiometric, with a boron-to-nitrogen (B/N) ratio of 1.6.

Elemental depth profiles for the ion-beam-deposited BN film on silicon as a function of sputtering time were obtained from AES analysis (Fig. 4.5) [4.6, 4.7]. The boron and nitrogen content rapidly increased in the first minute of sputtering, but the oxygen and carbon content decreased in the first 1 to 2 min and remained constant thereafter. The BN film deposited on silicon had a B/N ratio of about 2. Thus, XPS and AES analyses clearly revealed that BN was nonstoichiometric and that small amounts of oxides and carbides were present on the surface and in the bulk of the BN film. Contaminants such as carbides (e.g., B_4C) and oxides may have been introduced and absorbed into the BN film during ion beam deposition.

The BN films deposited on silicon substrates were probed by using secondary ion mass spectroscopy [4.6, 4.7]. The spectra indicated the presence of the following secondary ions: B^+, B_2^+, C^+, O^+, Si^+, Si_2^+, and SiO^+. The peak observed at 14 atomic mass units (amu) could result from N^+, CH_2^+, and SiO_2^+. Additional peaks at 24 and 25 amu were related to BN^+ and thus supported the XPS data. The SiO^+ signal was associated with the oxide present at the BN-silicon interface. AES depth profiles similar to Fig. 4.5 were obtained for a 116-nm-thick BN film deposited on indium phosphide (InP) and for a 129-nm-thick BN film deposited on gallium arsenide (GaAs) [4.7].

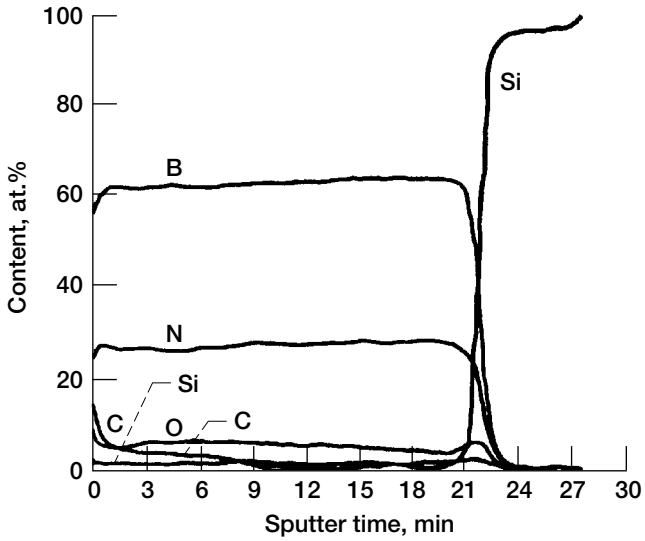

Figure 4.5.—AES elemental depth profiles as function of sputtering time for BN films ion beam deposited on silicon. Deposition temperature, 200 °C; ion beam energy, 150 eV.

Oxide ceramics.—Analogy between adhesion and friction was also found with oxide ceramic–metal couples, such as manganese-zinc (Mn-Zn) ferrite (Fig. 4.6). The contaminant layers on the as-received surfaces of Mn-Zn ferrite–metal couples reduced adhesion and friction. In this case, adhesion and friction did not depend on the material properties, such as shear modulus. Adhesion and friction were greater with the sputter-cleaned surfaces than with the as-received surfaces and, again, could be correlated with the Young's and shear moduli for the metals, as described in Chapter 3. Contaminants are weakly bound to the surfaces because the binding is physical rather than chemical. Under actual sliding conditions the contaminant surface layers may be removed by repeated sliding, making direct contact of the fresh, clean surfaces unavoidable [4.1, 4.2]. For example, when a tungsten carbide (WC)-coated ring was brought into contact with a sapphire (Al_2O_3) ring in air, the coefficient of friction increased as the number of passes increased, as shown in Fig. 4.7. Here, the coefficient of friction was not only high but erratic as well between 300 and 1600 passes. A plausible explanation is that the contaminant surface layers were removed by the repeated reciprocating sliding, allowing direct contact of the fresh, clean surfaces and increasing the coefficient of friction. Thus, the coefficient of friction of the sapphire-WC couple is also dependent on surface condition.

Debris generated by sliding action provides a useful history of the wear process. In addition to the quality and size of the wear debris particles, microscopic observation of their nature and shape yielded much more useful information [4.8, 4.9]. Scanning electron microscope (SEM) analysis of the wear scar produced on the sapphire ring by the sliding action revealed that the entire wear scar was generally smooth (Fig. 4.8). Most wear debris accumulated outside the wear scar and generally consisted of individual, fine (submicrometer and micrometer) particles. The friction behavior of an Si_3N_4 flat in contact with an Si_3N_4 pin in air was similar to the friction behavior of sapphire on tungsten dispersed with carbides.

Figure 4.9 shows another example [4.10]. When a natural diamond pin was in repeated sliding contact with a diamond film in ultrahigh vacuum, the coefficient of friction increased as the number of passes increased, reaching an equilibrium value after a certain number of passes. Again, repeatedly sliding the pin over the same track in ultrahigh vacuum had removed some contaminant surface film from the contact area. Stronger interfacial adhesion resulted between the diamond pin and the diamond film, raising the coefficient of friction.

4.2.2 Adsorbed Oxygen

Most gases, with the exception of the noble gases, adsorb readily to clean metal surfaces [4.1]; and many adsorb to nonmetals, such as silicon carbide (SiC), as well. Adhesion and friction are so sensitive to the presence of these gases, both qualitatively and quantitatively, that even hydrogen and fractions of a monolayer of other gases exert an effect. Practically all published works agree that extremely

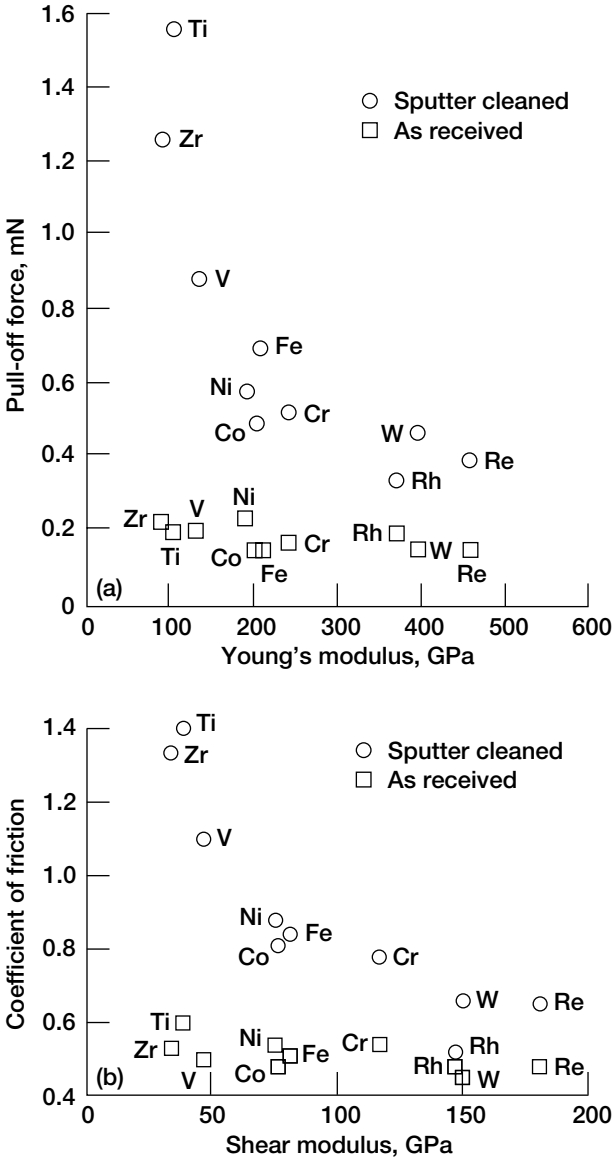

Figure 4.6.—Pull-off force (adhesion) as function of Young's modulus (a) and coefficient of friction as function of shear modulus (b) of metals in contact with polycrystalline Mn-Zn ferrite in ultrahigh vacuum.

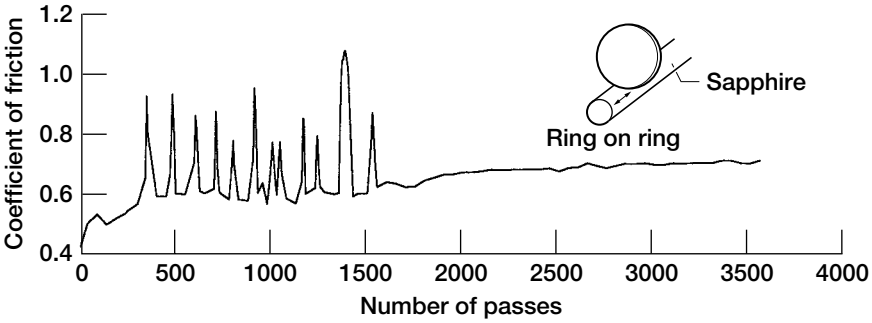

Figure 4.7.—Coefficient of friction as function of number of passes for sapphire (Al_2O_3) sliding against tungsten coating with dispersed carbides chemically vapor deposited on molybdenum in air. Reciprocating motion; load, 3 N; sliding velocity, 86 mm/min; track length, 2 mm; air environment; room temperature; relative humidity, 5.9%; cleaning agent, 1,1,1-trichloroethane.

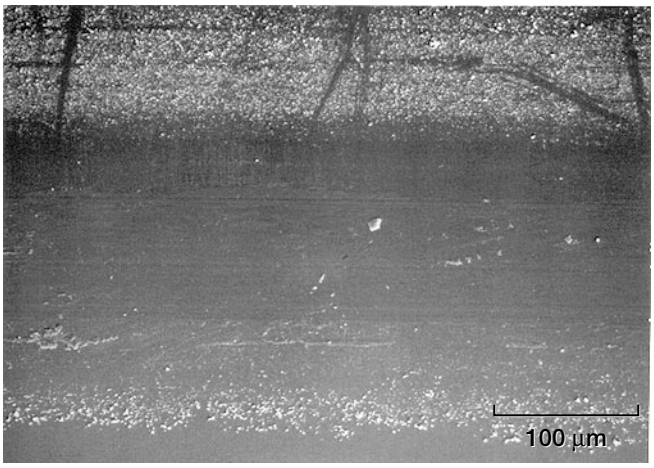

Figure 4.8.—Wear scar produced on Al_2O_3 ring by sliding contact in air. (The friction trace is shown in Fig. 4.7.)

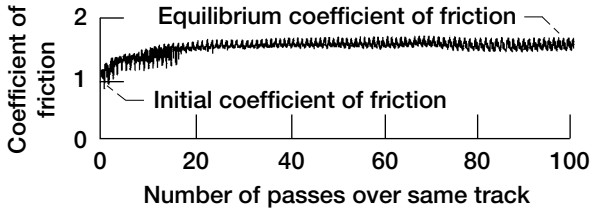

Figure 4.9.—Typical friction trace for bulk diamond pin in sliding contact with diamond film deposited on α-SiC substrate in vacuum.

small amounts of oxygen or other contaminant gases can greatly reduce the adhesion between metals [4.11–4.15]. However, there are situations where some amounts of oxides or a monolayer of oxygen when adsorbed can increase adhesion and friction.

On clean surface.—At room temperature and low pressures oxygen generally adsorbs on a clean SiC surface to an equilibrium layer thickness of no more than two monolayers [4.16]. For example, AES analysis has indicated that an SiC surface exposed to gaseous oxygen at 1.3 Pa and 25 °C for 1 hr will be covered with silicon oxide as well as with a simple adsorbed oxygen film [4.17]. Figure 4.10 shows the effect that such exposure has on friction behavior [4.18]. The presence of oxygen on the surfaces has reduced the coefficient of friction to two-thirds of that observed for the clean surfaces in contact. These sliding friction experiments were conducted with a single-crystal SiC pin in sliding contact with a single-crystal SiC disk in ultrahigh vacuum. The basal planes of both the pin and disk specimens were parallel to the sliding interface. The friction data presented in Fig. 4.10 were obtained as a function of the number of passes over the same track for argon-sputter-cleaned surfaces and for surfaces containing adsorbed oxygen. At a load of 0.3 N the adsorbed film gave the lower coefficient of friction after one to three passes of the pin. Friction markedly increased when the number of passes was increased from three to four, but beyond four passes the coefficients of friction were almost the same as those for sputter-cleaned SiC. This marked change in friction behavior is believed to be due to the breakdown of the adsorbed oxygen film by sliding action. At a load of 0.1 N, however, the adsorbed oxygen film did not break down for at least 20 passes.

On oxygen-ion-bombarded surface.—An argon-sputter-cleaned SiC surface was bombarded with oxygen ions at a 1000-V potential under a pressure of 1.3 Pa at 25 °C for 30 min. The AES spectrum of this surface (Fig. 4.11(a)) has three characteristic peaks: silicon peaks at 68 and 82 electron volts (eV), a carbon peak at 272 eV, and an oxygen peak at 516 eV [4.18]. The silicon peaks have two regions (I and II in the figure), which reflect the contribution to the valence band of silicon and oxygen bonding and nonbonding molecular orbitals [4.17]. The contribution from silicon-silicon bonds, which appeared at 92 eV, is not shown in this spectrum. Thus, the oxygen-ion-bombarded SiC surface seems to have been covered by

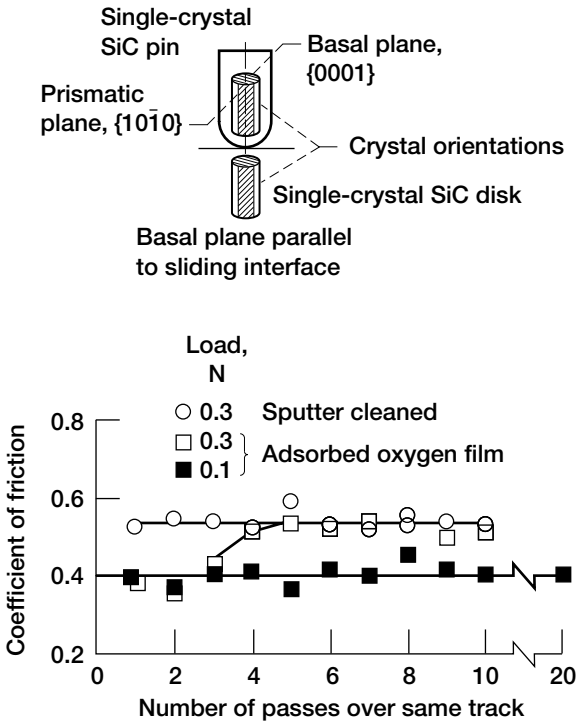

Figure 4.10.—Average coefficient of friction, obtained from maximum peak heights in friction trace, as function of number of passes of SiC pin across SiC {0001} disk. Oxygen adsorption conditions (disk and pin), 1.3 Pa and room temperature for 1 hr.

an SiO layer and, above that, an SiO_2 outer layer. The carbon peak, which was of the SiC type, is nearly undetectable in Fig. 4.11(a).

A sputter-cleaned and then oxygen-ion-bombarded SiC surface was exposed to oxygen at 1.3 Pa for 10 min. The Auger spectrum of this surface (Fig. 4.11(b)) shows the silicon peak to be at 78 eV. The position of the peak reflects the contribution to the valence band of silicon and oxygen nonbonding molecular orbitals [4.17]. The carbon peak is small, as in Fig. 4.11(a).

The coefficients of friction obtained for the oxygen-ion-bombarded SiC surfaces (Fig. 4.11(c)) were slightly higher than those obtained for sputter-cleaned SiC surfaces (Fig. 4.10). Also, at a load of 0.3 N the adsorbed film on the oxygen-ion-bombarded surface gave a fairly constant low coefficient of friction throughout the experiment without breaking down.

On reacted oxide surface.—To form a reacted oxide film on a single-crystal SiC surface, the SiC was first exposed to air at atmospheric pressure and 700 °C

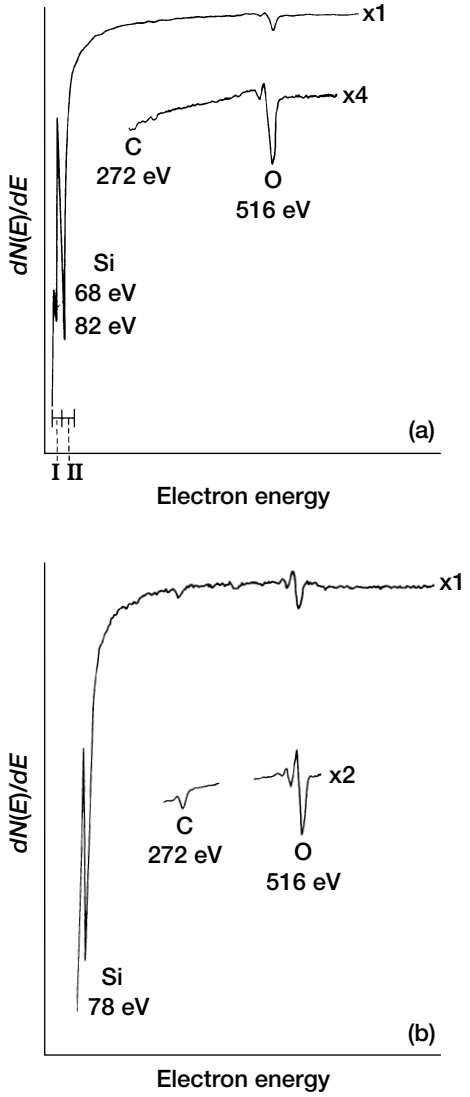

Figure 4.11.—Auger spectra and coefficients of friction for single-crystal SiC {0001} surfaces. (a) Auger spectrum for surface with ion-bombarded oxygen film. (b) Auger spectrum for surface with adsorbed oxygen film on ion-bombarded oxygen film. (c) Coefficients of friction for both surfaces.

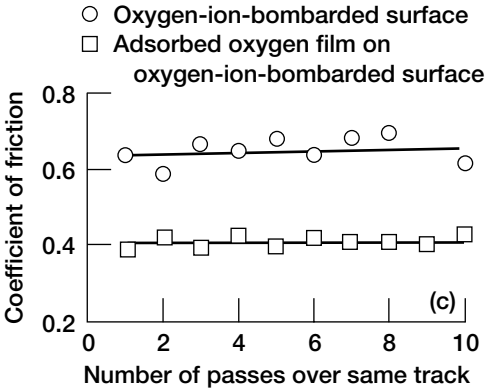

Figure 4.11.—Concluded. (c) Coefficients of friction.

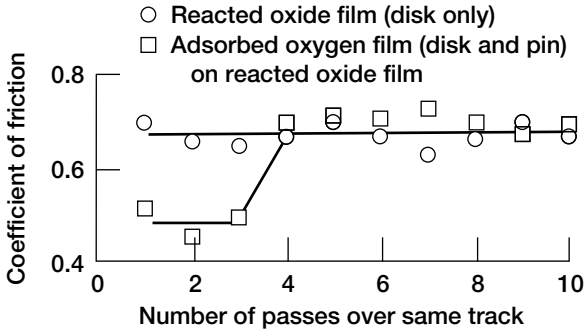

Figure 4.12.—Average coefficients of friction for single-crystal SiC {1} surfaces with sputter-cleaned, reacted oxide film with and without adsorbed oxygen film.

for 10 min [4.18]. Then, the oxidized SiC surface was argon ion sputter cleaned in vacuum. After sputter cleaning the carbon peak was barely discernible in the AES spectrum. An oxygen peak and a chemically shifted silicon peak (at 82 eV) indicated a layer of SiO_2 on the SiC surface. After oxygen adsorption on the reacted oxide film, a slightly higher oxygen AES peak was present on the SiC surface than on the clean reacted oxide film.

Figure 4.12 presents the friction data obtained for surfaces with a reacted oxide film and with an adsorbed oxygen film on the reacted oxide. The adsorbed oxygen film gave a lower coefficient of friction during the first three passes but the same values beyond three passes as did the clean reacted film. Again, the marked increase in friction beyond three passes is believed to be due to sliding action breaking down the adsorbed oxygen film.

Figures 4.13 and 4.14 summarize the coefficients of friction measured at a load of 0.3 N with a single sliding pass for SiC-to-SiC and SiC-to-titanium interfaces with reacted, ion-bombarded, and adsorbed oxygen or nitrogen films [4.18]. The effects of oxygen interactions on the friction behavior were generally the same for both couples. The reacted oxide and oxygen-ion-bombarded surfaces interacted with the SiC surfaces to produce two effects: (1) SiC oxidized and formed a protective oxide surface layer and (2) the layer increased the coefficients of friction for both couples.

The effects of oxygen in increasing friction are related to the relative chemical thermodynamic properties of silicon, carbon, and titanium to oxygen. Table 4.1 presents free energies of formation for silicides, oxides, carbides, and nitrides [4.19, 4.20]. The greater the degree of oxidation or oxygen implantation by ion bombardment, the more chemically active the surface (Table 4.1) and the higher the coefficient of friction (Fig. 4.13). In such a situation oxygen will tend to chemically bond to the surface.

By contrast, adsorption of oxygen on argon-ion-sputter-cleaned, oxygen-ion-bombarded, and reacted oxide surfaces generally decreased the coefficient of friction (Figs. 4.14). Also, adsorption of nitrogen on argon-ion-sputter-cleaned surfaces decreased the coefficient of friction (Fig. 4.14). When oxygen and nitrogen adsorb on the surface, the forces of attraction between the adsorbing gas and the SiC surface seem to be relatively weak. Thus, the adsorption of nitrogen or oxygen generally reduces adhesion and friction.

4.2.3 Defined Exposure to Oxygen

As discussed in the previous section, the coefficient of friction is strongly affected by gas interactions with the surface, such as the adsorption of a species (physically or chemically adsorbed material) or the chemical reactions of the surface with a species.

Figure 4.15 presents the coefficients of friction as a function of the d valence bond character of various transition metals in contact with nickel-zinc (Ni-Zn) ferrite. Both the argon-ion-sputter-cleaned metal and the ferrite were exposed to 1000 langmuirs (1×10^{-6} torr-s) of oxygen gas in vacuum at 1.33×10^{-4} Pa [4.21]. At completion of the exposure the vacuum system was evacuated to 30 nPa or lower for the sliding friction experiments.

Figure 4.15 also presents comparative data for clean metals in contact with clean Ni-Zn ferrite. The adsorption of an oxygen monolayer on argon-sputter-cleaned metal and ferrite surfaces produced two effects: (1) the metal oxidized and formed an oxide surface layer and (2) the oxide layer increased the coefficients of friction for the ferrite-to-metal interfaces. Oxygen adsorption had the same effect on the adhesion and friction of Ni-Zn ferrite–metal contacts as was observed for metals in sliding contact with Mn-Zn ferrite (see Chapter 3). That is, oxygen

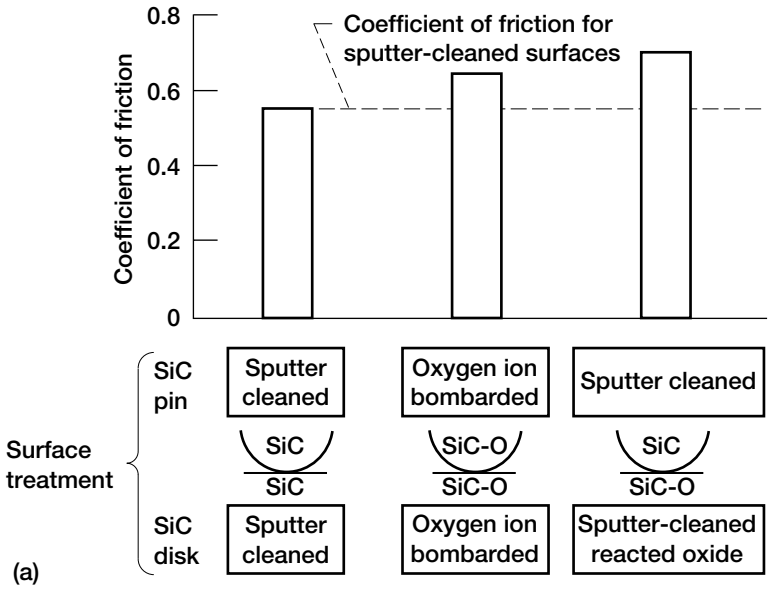

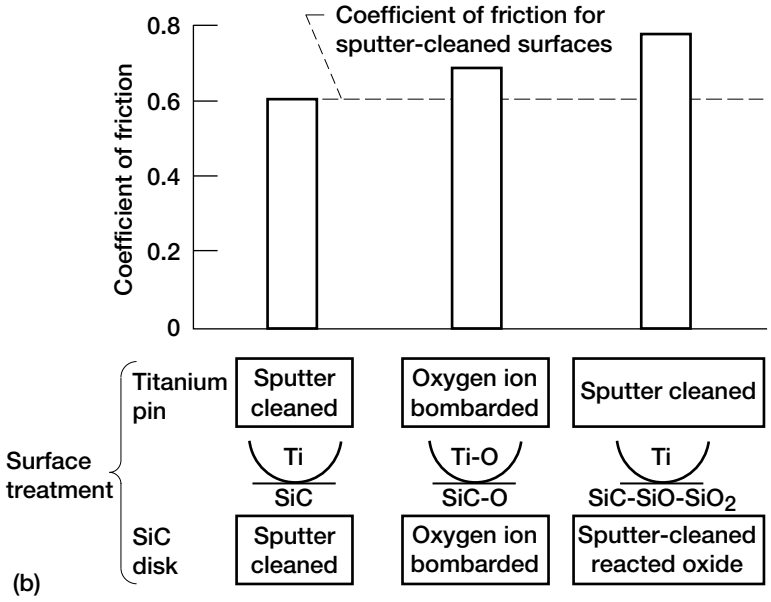

Figure 4.13.— Average coefficients of friction for SiC-to-SiC (a) and SiC-to-titanium (b) contacts after various surface treatments. Single-pass sliding.

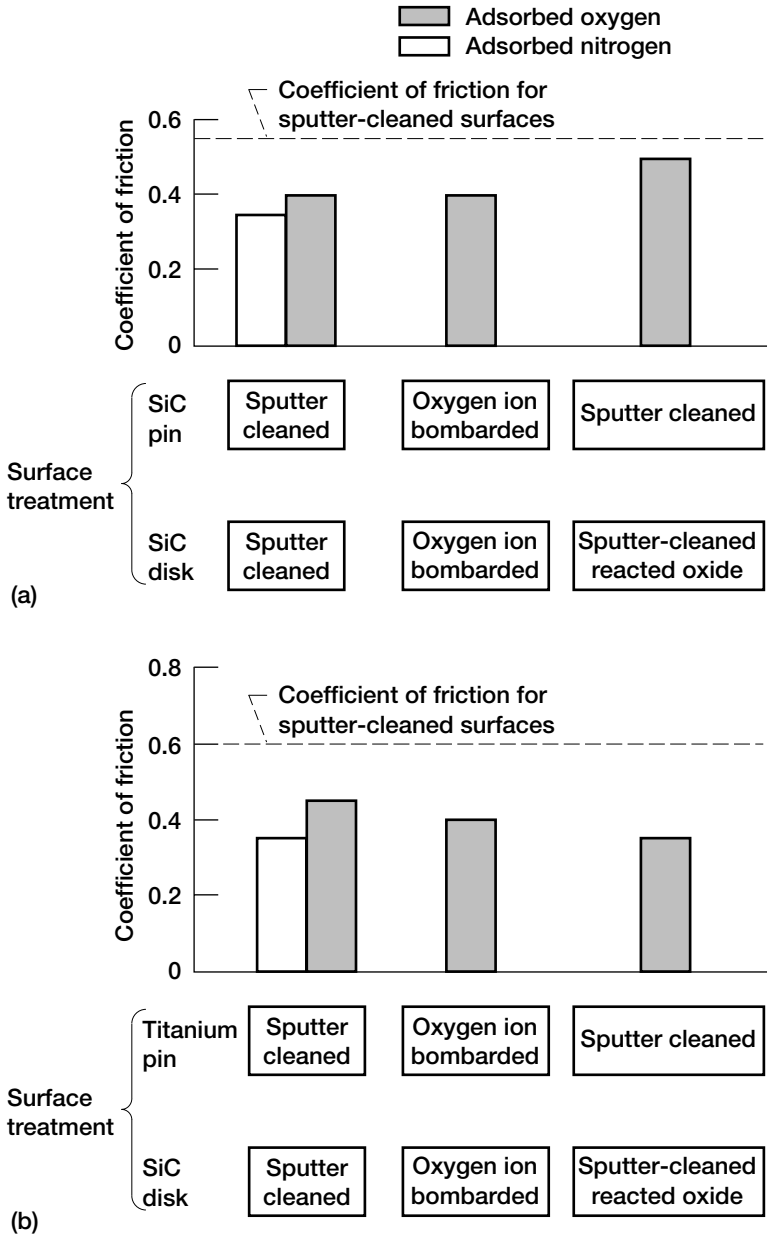

Figure 4.14.— Average coefficients of friction for SiC-to-SiC (a) and SiC-to-titanium (b) contacts with adsorbed oxygen and nitrogen films after various surface treatments. Single-pass sliding.

TABLE 4.1.—FREE ENERGY OF FORMATION

Formula	Free energy of formation	
	kcal/mole	J/mole
SiC	–26.1	-109×10^3
SiO	–32.77	–137
SiO_2	–192.4	–805
CO	–32.81	–137
CO_2	–94.26	–394
Si_3N_4	–154.7	–647
TiSi	–31.0	–130
TiC	–53	–222
TiO	–116.0	–485
TiO_2	–203.8	–853
TiN	–66.1	–277

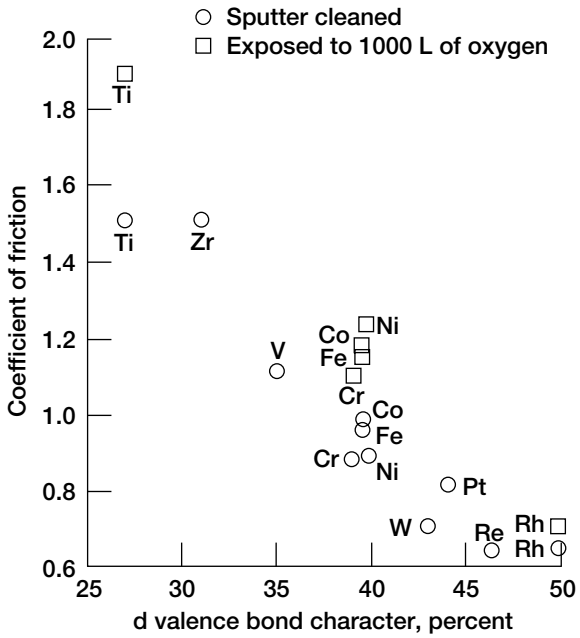

Figure 4.15.—Effect of adsorbed oxygen on friction for various metals in sliding contact with Ni-Zn ferrite. Single-pass sliding; sliding velocity, 3 mm/min; load, 0.05 to 0.2 N; vacuum, 30 nPa; room temperature.

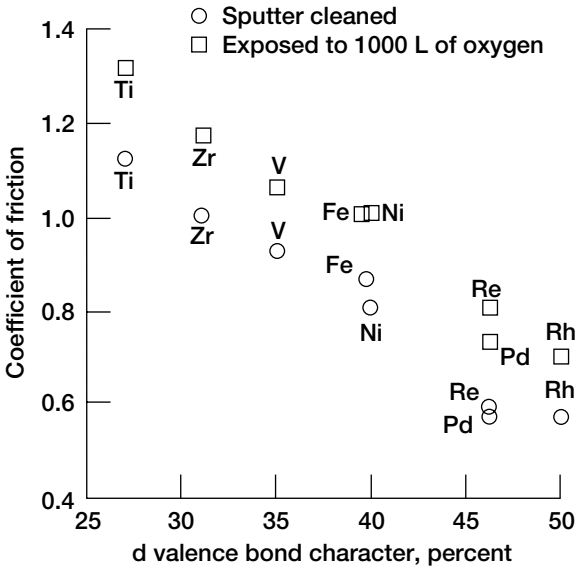

Figure 4.16.— Effect of adsorbed oxygen on friction for various metals in sliding contact with BN. Single-pass sliding; sliding velocity, 3 mm/min; load, 0.05 to 0.2 N; vacuum, 30 nPa; room temperature.

exposure strengthened metal-to-ferrite adhesion and increased friction. The enhanced bonding of the metal oxide to the ferrite may be due to a complex oxide forming on contact.

Figure 4.16 presents the coefficients of friction for clean metals in contact with BN coatings after exposure to oxygen gas [4.6]. The data reveal that the adsorption of oxygen on the surfaces of argon-sputter-cleaned metals and BN coatings produced two effects: (1) the metal and BN oxidized and formed an oxide surface layer and (2) the oxide layers increased the coefficient of friction for metal-to-BN interfaces. Thus, the oxygen exposure strengthened metal-to-BN adhesion and increased friction.

4.2.4 Humidity

Effect on adhesion.—The concentration of humidity (water vapor) in the atmosphere has a marked effect on a material's mechanical, chemical, and tribological properties. Figure 4.17 presents the pull-off forces necessary to separate a hemispherical Si_3N_4 pin in contact with an Si_3N_4 flat in dry, moist, and water-vapor-saturated nitrogen atmospheres [4.22]. Adhesion (pull-off force) remained low at relative humidities below 80% but rose rapidly above 80%. There was no change

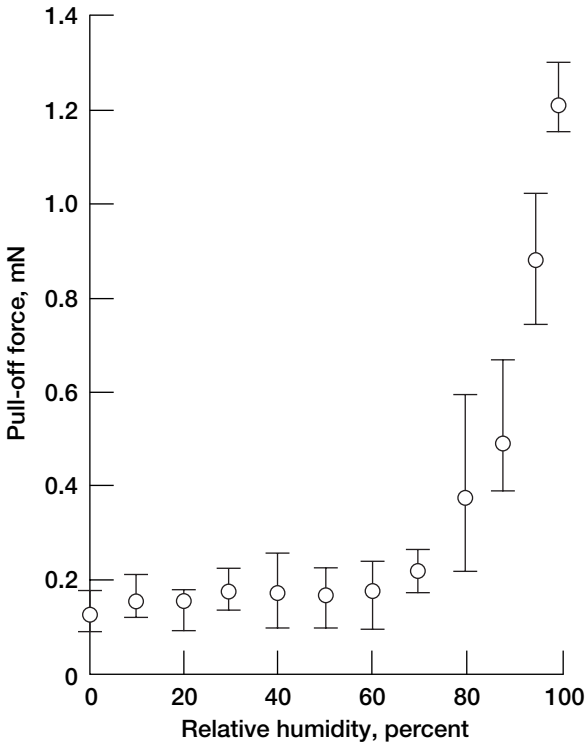

Figure 4.17.—Pull-off force (adhesion) as function of relative humidity for hemispherical Si_3N_4 pin in sliding contact with Si_3N_4 flat in nitrogen atmosphere.

in adhesion with normal load between 0.2 and 0.8 mN in dry, moist, and water-vapor-saturated nitrogen.

Probably, the greater adhesion observed in the water-vapor-saturated nitrogen atmosphere arose primarily from the surface tension effects of a thin water film adsorbed on the Si_3N_4 surfaces. The happenings at the interface may be visualized as follows:

1. An Si_3N_4 pin was essentially in elastic contact with an Si_3N_4 flat surface with a thin water film between them (Fig. 4.18(a)).
2. When the normal load was removed and the elastic stresses within the bulk of the specimens were released, the interfacial junctions were broken one by one.
3. When the pin (of radius *R*) detached from the flat (Fig. 4.18(b)), the applied separation force was balanced by the surface tension of a thin water film resisting surface extension.

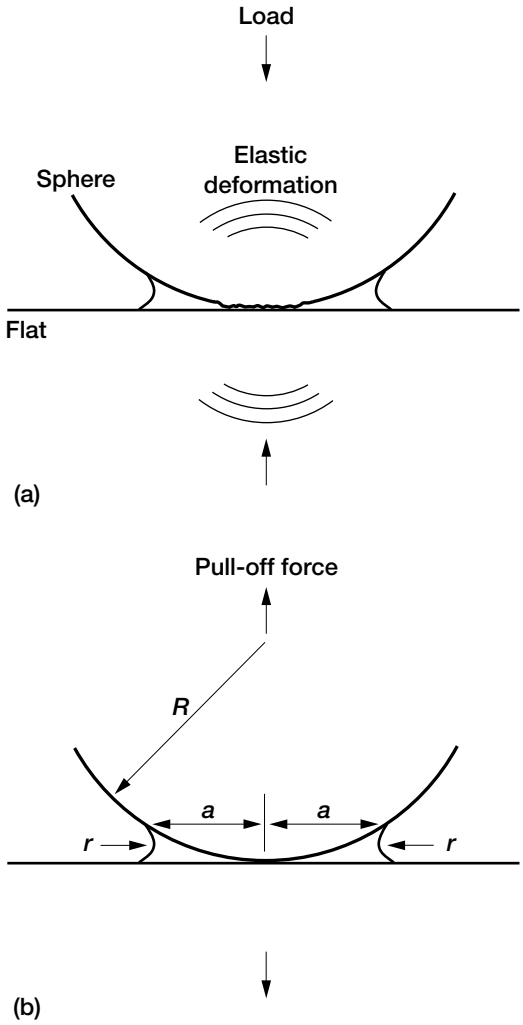

Figure 4.18.—Meniscus formed at contact area between spherical and flat surfaces. (a) Contact. (b) Separation.

4. Suppose the liquid collected to form a pool at the tip of the hemispherical pin. (The radius of curvature of the meniscus profile is r.) If the meniscus were extremely small ($r << R$) and the liquid completely wetted the surface (i.e., zero contact angle), the pressure p inside the liquid would be less than atmospheric pressure by approximately T/r, where T is the surface tension of the liquid. This low pressure would act over an area πa^2 of the water pool, giving a total adhesive force of $p\pi a^2$ (i.e., $\pi a^2 T/r$). To a close approximation

$a^2 = 2R \times 2r$, where R is the radius of curvature of the spherical surface. The resulting adhesive force would be [4.23, 4.24]

$$Z = 4Rr\pi \frac{T}{r} = 4\pi RT \tag{4.1}$$

Adhesion is thus independent both of water film thickness and applied normal load. The surface tension calculated from these experimental results (Fig. 4.17) is 58×10^{-5} to 65×10^{-5} N/cm. The accepted value for water is 72.7×10^{-5} N/cm. This discrepancy may be due to the surface roughness and irregular roundness or flatness of the Si_3N_4 specimens. Surface irregularities can affect the radii of curvature of the hemispherical pin and the meniscus.

The results shown in Fig. 4.17 are of great interest. In practical fields, such as information storage systems, the role humidity plays in adhesion and friction is relevant to understanding the tribological problem. Therefore, a case study was conducted that shows the important role water vapor plays in the friction of a magnetic tape sliding against a ferrite (a magnetic head material) pin.

The effects of humidity in moist nitrogen on the friction and deformation behavior of polymeric magnetic tapes in contact with a polycrystalline Ni-Zn ferrite hemispherical pin [4.25] were examined in the case study. Experiments were conducted with loads to 1.0 N at sliding velocities to 6 mm/min in single-pass and multipass sliding at room temperature. Multipass sliding experiments were conducted in reciprocating motion.

Figure 4.19 shows the layer structure of the polymeric magnetic tape. Primary components of the magnetic layer were the magnetic oxide particles, the binder, the lubricant, the dispersant, and other minor additives. The magnetic tapes used in this investigation contained powders coated on a polyester film backing (film thickness, 23 μm; film width, 12.7 mm). The two kinds of tapes, designated 1 and 2, used in this investigation were made with polyester-polyurethane binders, the most

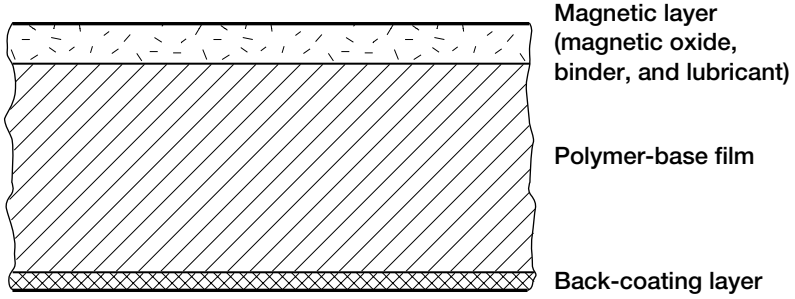

Figure 4.19.— Schematic of magnetic tape.

widely used binders for magnetic tape applications. The magnetic layers contained magnetic oxide (γ-Fe_2O_3) particles equal to 70% of the layer by weight and as much as 60% by volume.

Effect on friction and deformation.—Traces of friction at various loads on the tape as a function of sliding time are relatively smooth, with no evidence of stick-slip. The coefficient of friction was not constant but decreased as the load increased to 0.25 N (Fig. 4.20(a)). As the load increased above 0.25 N, however, the coefficient of friction increased. When repeated passes were made (Fig. 4.20(b)), the coefficient of friction for the tape generally exhibited small changes at loads less than 1.0 N. The data of Fig. 4.20, particularly part (a), raise the question of how the interface deforms with sliding action.

The tracks on the tape made by the ferrite pin looked different at various loads when examined by optical and scanning electron microscopy. Essentially no detectable wear track existed on the tape surface at 0.1 N. The wear track was similar to that shown in Fig. 4.21(a), the surface of as-received magnetic tape (tape 1). At 0.25 N and above the sliding action produced a visible wear track on the magnetic tape, similar to that shown in Fig. 4.21(b). This scanning electron micrograph clearly reveals a degree of plastic deformation at the asperity tips on the magnetic tape. Thus, although sliding occurred at the interface, both the tape and the Ni-Zn ferrite pin were elastically deformed at loads to 0.25 N. At 0.25 N

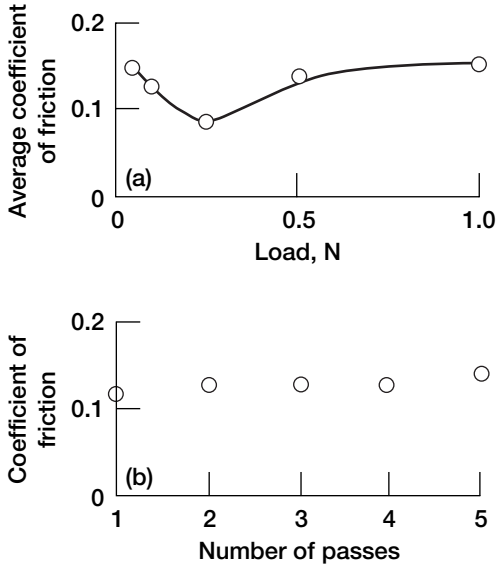

Figure 4.20.—Coefficient of friction as function of load (a) and number of passes (b) for Ni-Zn ferrite sliding on magnetic tape (tape 1) in laboratory air.

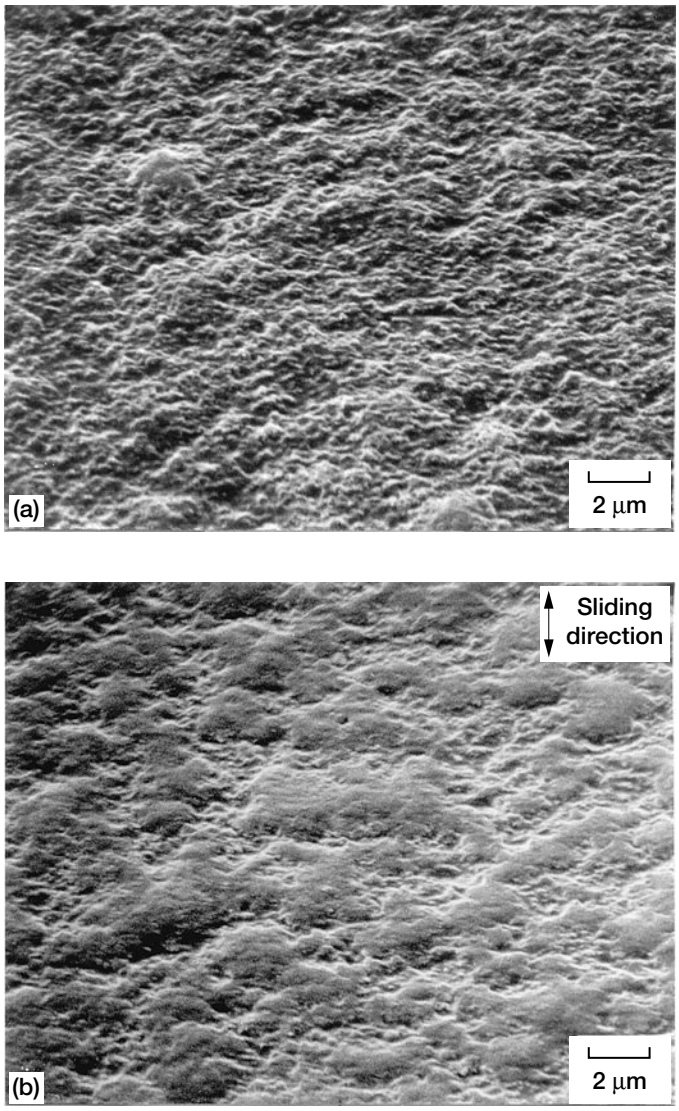

Figure 4.21.—Scanning electron micrographs of as-received surface (a) and wear track (b) on magnetic tape (tape 1) after five passes of Ni-Zn ferrite pin. Normal load, 1 N; sliding velocity, 1.5 mm/min; relative humidity, 40%; room temperature; laboratory air.

and above the tape deformed plastically, but the Ni-Zn ferrite pin primarily deformed elastically. Figure 4.21(b) shows the blunt appearance of the asperities on the wear track after five sliding passes at 1.0 N. This bluntness resulted primarily from plastic deformation.

From the nature of deformation at the interface the friction behavior of the hemispherical Ni-Zn ferrite pin and the magnetic tape can generally be divided into two categories (i.e., elastic and plastic contact). In the elastic contact region the friction decreases as the load increases. The relation between coefficient of friction μ and load W is given by an expression of the form $\mu = KW^{-1/3}$, where K is a constant [4.26, 4.27]. The exponent can be interpreted simply as arising from an adhesion mechanism, with the contact area being determined by elastic deformation.

For example, the coefficients of friction for the polyester tape backing in contact with the Ni-Zn ferrite pin decreased as the load increased. That is, with sliding, both the polyester backing and Ni-Zn ferrite pin surfaces deformed elastically [4.28]. By contrast, when deformation was plastic, the coefficient of friction for a hard, spherical solid pin in contact with a soft, solid tape increased as the load increased. Figure 4.20(a) presents a typical example of this at loads of 0.25 N and above [4.28]. The role of deformation in friction will be discussed in more detail in Chapter 5.

Effect on plastic deformation and softening.—The coefficient of friction measured for tape 2 was 0.14 in dry nitrogen at a load of 0.5 N (Fig. 4.22(a)). The atmosphere was then humidified to the desired relative humidity (up to 78%) by admitting humid nitrogen into the system. On humidifying (open symbols) the coefficient of friction remained low below 40% relative humidity but then increased rapidly. On dehumidifying (solid symbols) the coefficient of friction decreased rapidly between 78% and 40% relative humidities and then remained low. The friction behavior of the tape on dehumidifying was similar to that on humidifying.

At 0.25 N (Fig. 4.22(b)) the results were consistent with those at 0.5 N. At both 0.25 and 0.5 N the sliding action produced a visible wear track on the magnetic tape. The question was, Would the interface deform differently in high humidity than in dry nitrogen with sliding action (i.e., would the tape deform readily in a moist atmosphere)? To examine the deformation behavior of the tape surface, multipass sliding friction experiments were conducted with magnetic tapes in sliding contact with polycrystalline Ni-Zn ferrite pins in both dry and humid nitrogen at 78% relative humidity.

Figure 4.23 presents the coefficients of friction for magnetic tape (tape 2) in nitrogen at 78% relative humidity as a function of the number of repeated passes. After 50 passes the coefficient of friction decreased slightly, but continuously, as the number of passes increased. However, the coefficient of friction measured in dry nitrogen was constant after 10 passes. These results suggest that a polymeric magnetic tape in contact with an Ni-Zn ferrite pin would deform plastically in humid nitrogen (78% relative humidity) more than it would in dry nitrogen.

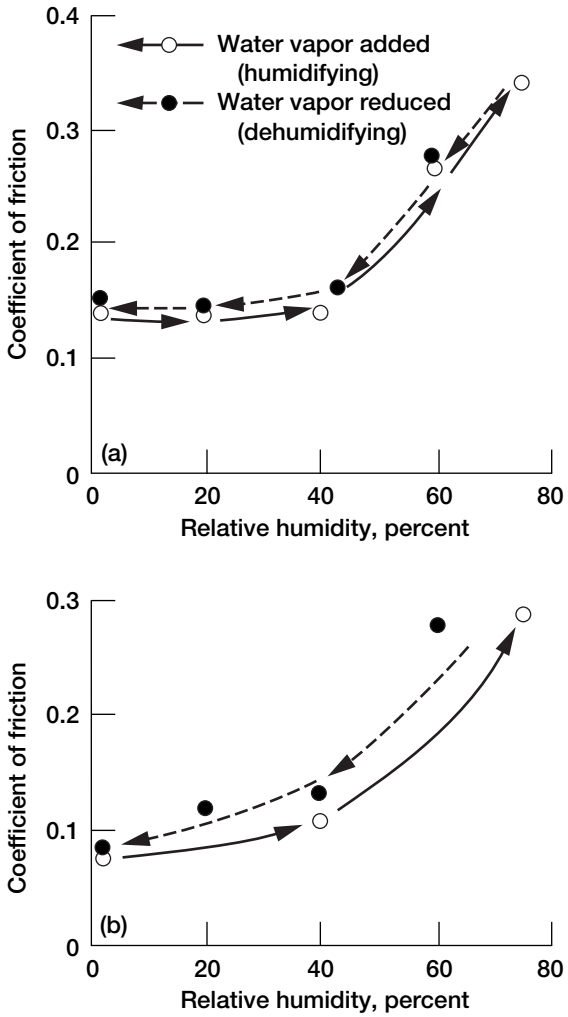

Figure 4.22.—Effect of humidifying and dehumidifying on friction of magnetic tape (tape 2) in sliding contact with Ni-Zn ferrite pin at normal loads of 0.5 and 0.25 N. Sliding velocity, 0.1 mm/s; room temperature; environment, nitrogen. (a) Normal load, 0.5 N. (b) Normal load, 0.25 N.

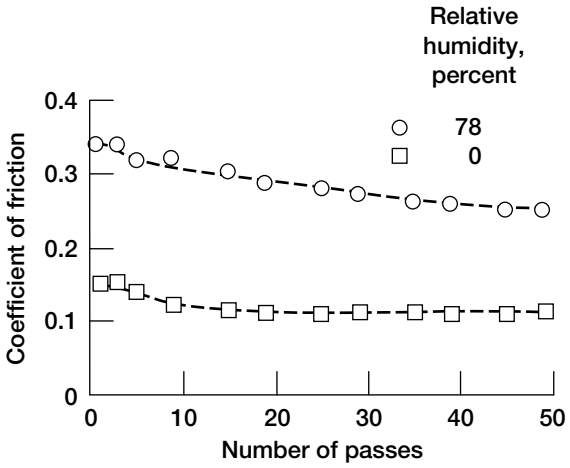

Figure 4.23.—Coefficient of friction as function of number of passes for magnetic tape (tape 2) in sliding contact with Ni-Zn ferrite pin. Normal load, 0.5 N; sliding velocity, 0.1 mm/s; room temperature; environments, dry and humid nitrogen.

To determine tape surface deformation with sliding action in both dry and humid nitrogen, the wear tracks on the tape were examined by scanning electron microscopy after 50 repeated passes. Figure 4.24 presents scanning electron micrographs of the as-received magnetic tape surface and the wear tracks generated in dry nitrogen and in humid nitrogen (78% relative humidity). The as-received tape surface (Fig. 4.24(a)) had the coarsest structure. Both wear tracks (Figs. 4.24(b) and (c)) clearly reveal a degree of plastic deformation at the asperity tips. Considerable plastic flow occurred in the tape during sliding contact with the Ni-Zn ferrite pin in humid nitrogen, much more than in the dry nitrogen. Softening of the tape surface due to the water vapor in the humid nitrogen caused the plastic deformation.

Effect on elastic deformation.—At loads of 0.05 and 0.1 N both the tape and the Ni-Zn ferrite primarily deformed elastically and the sliding occurred at the interface. Figure 4.25 presents the coefficients of friction as a function of relative humidity. On humidifying (open symbols) the coefficient of friction increased linearly with increases in relative humidity. On dehumidifying (solid symbols) the coefficient of friction decreased linearly with decreases in relative humidity. The friction behavior of the tape on dehumidifying was similar to that on humidifying. The results at 0.05 N are consistent with those at 0.1 N.

Frictional response to humidity changes.—The first experiment looked at the change from a dry to a humid environment. A tape was preconditioned in dry nitrogen before each of forty-nine 90-s sliding passes. On each pass after 40 s of sliding in dry nitrogen the area around the tape–Ni-Zn ferrite pin contact (less than 100 mm^2) was flooded with nitrogen having 61% relative humidity. Figure 4.26

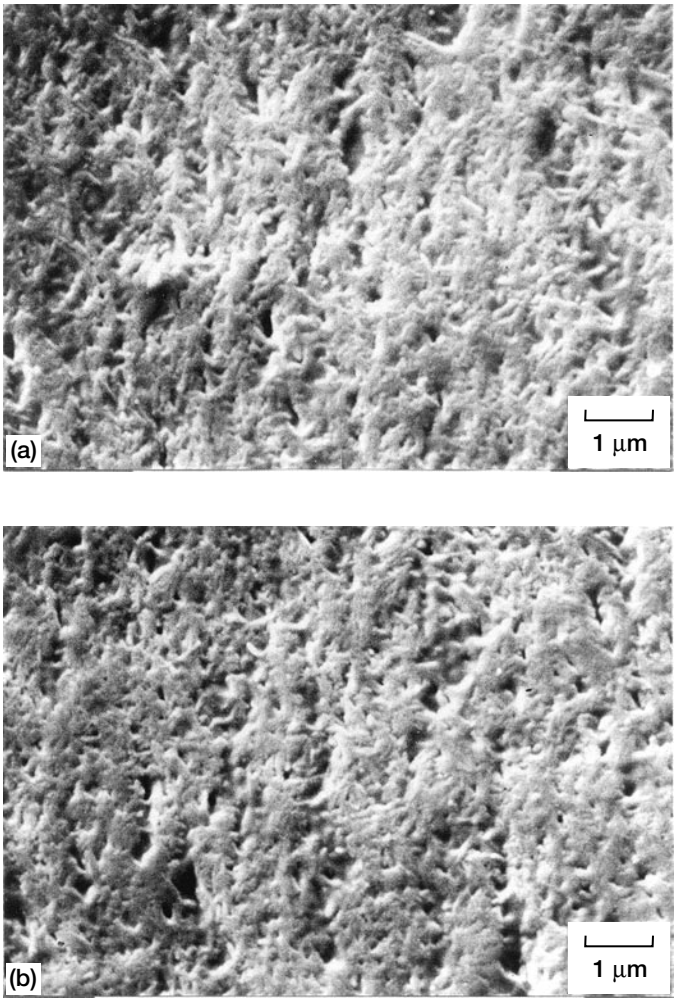

Figure 4.24.—Scanning electron micrographs of as-received surface and wear tracks on magnetic tape (tape 2) after 50 passes against Ni-Zn ferrite pin. Normal load, 0.5 N; sliding velocity, 0.1 mm/s; room temperature; environments, dry and humid nitrogen. (a) New tape (as-received surface). (b) Wear track obtained in dry nitrogen. (c) Wear track obtained in humid nitrogen (78% RH).

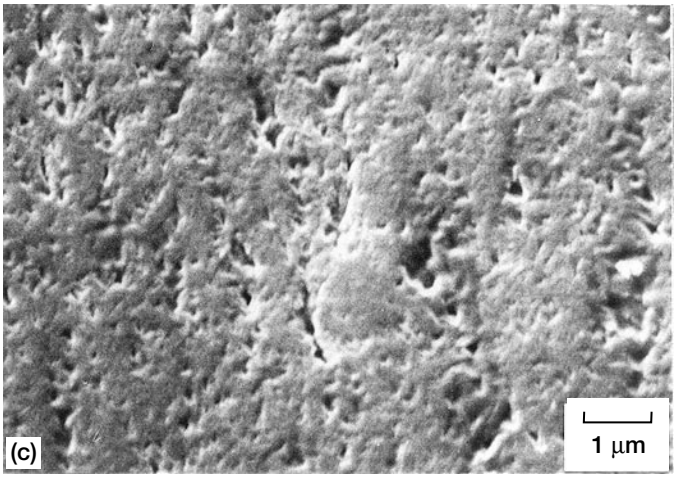

Figure 4.24.—Concluded. (c) Wear track obtained in humid nitrogen (78% RH).

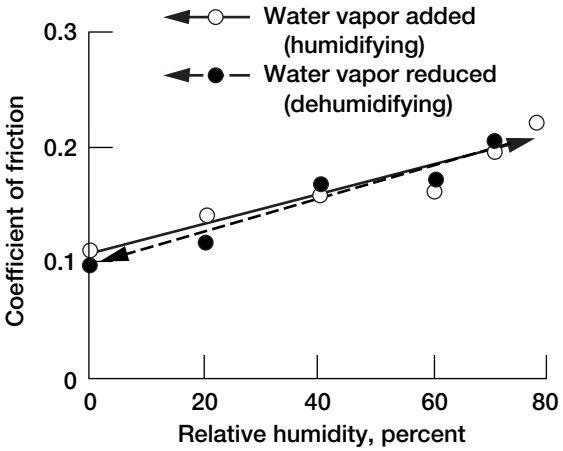

Figure 4.25.—Effect of humidifying and dehumidifying on friction of magnetic tape (tape 2) in sliding contact with Ni-Zn ferrite pin at normal load of 0.1 N. Sliding velocity, 0.1 mm/s; room temperature; environment, nitrogen.

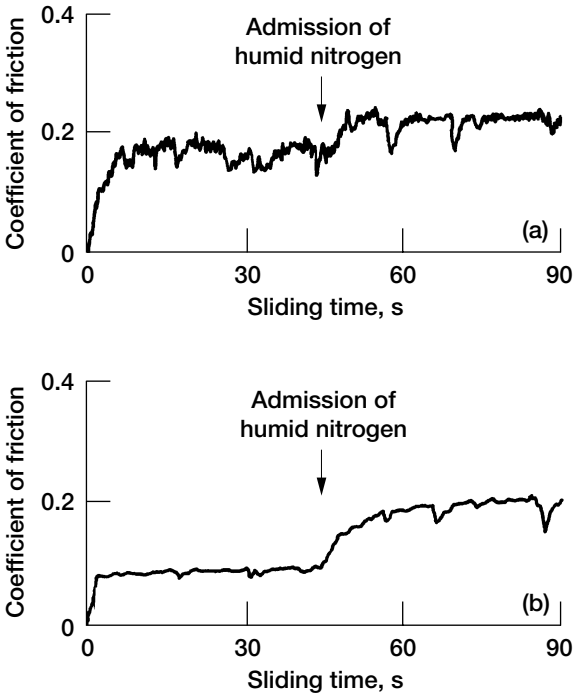

Figure 4.26.—Effect of humidity change due to admission of humid nitrogen (61% RH) on coefficient of friction for magnetic tape (tape 2) sliding against Ni-Zn ferrite pin. Normal load, 0.5 N; sliding velocity, 0.1 mm/s; room temperature; environment, nitrogen. (a) First pass. (b) Forty-ninth pass.

presents coefficient of friction as a function of sliding time under these environmental conditions. In the first pass, right after admitting humid nitrogen, the coefficient of friction increased. The coefficients of friction measured in the area flooded with humid nitrogen were 30 to 40% higher than those measured in dry nitrogen. With repeated sliding passes the tape exhibited about 2 to 2.5 times higher friction when local humidity was raised than it did in dry nitrogen.

The second experiment looked at the change from a humid to a dry environment. A tape was preconditioned in nitrogen with 63% relative humidity before each of forty-nine 90-s sliding passes. On each pass after 40 s of sliding in humid nitrogen the area around the tape–Ni-Zn ferrite pin contact was flooded with dry nitrogen. Figure 4.27 clearly shows another surprising aspect of humidity dependence. When the contact area was flooded with dry nitrogen, the coefficient of friction decreased dramatically, being 80% of the friction obtained in the humid nitrogen atmosphere in single-pass sliding and 60% in multipass sliding.

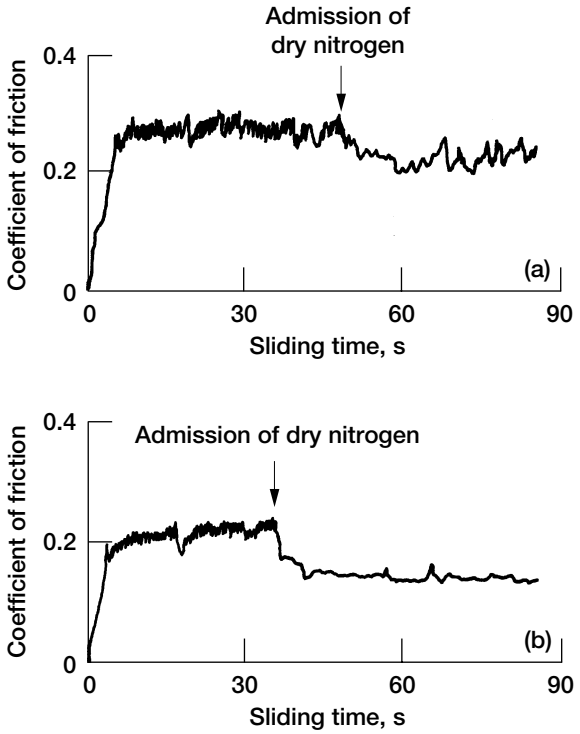

Figure 4.27.—Effect of humidity change due to admission of dry nitrogen on coefficient of friction for magnetic tape (tape 2) sliding against Ni-Zn ferrite pin. Normal load, 0.5 N; sliding velocity, 0.1 mm/s; room temperature; environment, nitrogen. (a) First pass. (b) Forty-ninth pass.

The third experiment studied two reversals in environment. The area surrounding the tape–Ni-Zn ferrite pin contact was flooded with dry nitrogen. At approximately 30 s of sliding time the supply of dry nitrogen was stopped and then humid nitrogen, at 61% relative humidity, was admitted to the contacting area for about 30 s. The supply of humid nitrogen was then stopped and dry nitrogen was again allowed to flow into the contact area. Figure 4.28 clearly indicates the marked increase in coefficient of friction as the humidity increased. Only a short transient time (~10 s) was needed for the friction to decrease or increase in relation to the humidity changes.

Mechanism of tape friction and humidity effect.—The previous sections have shown that sliding occurred primarily at the interface and that the coefficient of friction was greatly influenced by the interaction of the tape and Ni-Zn ferrite surfaces. When these surfaces are brought into elastic contact, interfacial adhesion can take place and shearing of adhesive bonds at the interface is responsible for

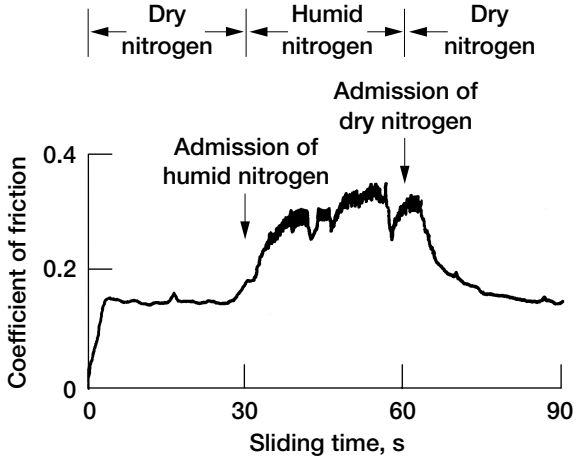

Figure 4.28.—Effect of humidity changes due to admission of humid or dry nitrogen on coefficient of friction as function of sliding time for magnetic tape (tape 2) sliding against Ni-Zn ferrite pin. Normal load, 0.5 N; sliding velocity, 0.1 mm/s; room temperature; environment, nitrogen; third pass.

friction. As Fig. 4.25 shows, the coefficient of friction increased linearly with increasing humidity and decreased when humidity was lowered. In elastic contact the changes in friction on humidifying and dehumidifying were reversible.

When an Ni-Zn ferrite pin was brought into sliding contact with an Ni-Zn ferrite flat, water adsorption on the surface did not affect the coefficient of friction, as shown in Fig. 4.29. There was no change in friction with relative humidity. The experiments with the ferrite-ferrite contact were identical to those with the tape-ferrite contact. Therefore, the effect of humidity on friction for the tape-ferrite contact, seen in Fig. 4.28, was primarily due to alteration of the tape surface. Humidity affects the friction behavior of a tape in elastic contact because it changes the chemistry and interaction of the tape. Most probably, the lubricant and binder in the tape react with the water vapor.

As Fig. 4.22 shows, when a tape was plastically deformed during sliding, the coefficient of friction remained low and constant below 40% relative humidity. There was no humidity effect on friction. Because the load applied to the contacting surfaces was sufficiently high and plastic deformation occurred, the Ni-Zn ferrite pin broke through the adsorbed water vapor film. The adhesive bonding at the contact, where fresh surfaces were continuously exposed through the water vapor film below 40% relative humidity, was similar to that in dry nitrogen.

As the relative humidity increased above 40%, however, the coefficient of friction increased rapidly (Fig. 4.22). The humidity softened the tape surface and

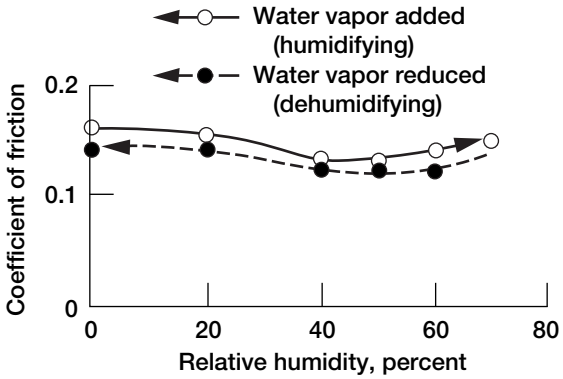

Figure 4.29.—Effect of humidifying and dehumidifying on friction of Ni-Zn ferrite pin in sliding contact with Ni-Zn ferrite flat. Normal load, 0.5 N; sliding velocity, 0.1 mm/s; room temperature; environment, nitrogen.

changed the chemistry and interaction of the tape. Probably, the lubricant reacted with the water vapor and the binder became less stable. Exposure to high humidity and elevated temperatures for several weeks can result in hydrolytic reaction of the tape-binder system [4.29]. The primary mechanism relevant to magnetic tape involves the scission of the chainlike polymer structure by the action of water, which effectively breaks the polymer into small fragments having low molecular weights.

The experiments described in this case study were conducted at room temperature, and the tape was exposed to humid nitrogen for less than 1 hr. Figures 4.22 and 4.25 show that friction reversed on humidifying and dehumidifying. Removing the adsorbed water vapor film from the tape and pin surfaces lowered the coefficients of friction to those before humidifying. Thus, exposing a tape to humid nitrogen for short periods at room temperature may result in a negligibly small amount of hydrolytic degradation of the tape binder. The scission of the chainlike polymer structure by the action of water vapor would also be negligible.

With the mechanical activity that takes place during sliding, however, water vapor adsorbed on the tape surface tends to promote chemical reaction and degradation of the tape long before the surface may otherwise be ready for such deterioration. Binder degradation can lead to deterioration of the mechanical properties.

We know that the surfaces of materials in sliding contact are highly strained by the mechanical activity that takes place. Under such conditions, on the surface and in the surficial layers of a tape with an adsorbed water vapor film, the binder and lubricant chemistry can be changed markedly by the strain. The higher the degree of strain, the lower the chemical stability of the binder system and the greater the hydrolytic reaction and degradation of the binder.

Similar phenomena have been observed with other materials. For example, the crystallinity and crystallographic orientation of a crystalline metal surface can be changed markedly by strain. The higher the degree of strain, the lower the recrystallization temperature. Consequently, high strain tends to promote recrystallization of a solid surface long before the surface may otherwise be ready for such recrystallization [4.30–4.32].

Furthermore, on the surface of an amorphous alloy (metallic glass), sliding is accompanied by a high degree of strain at room temperature, even when the sliding velocity is extremely low. This strain induces crystallization of the amorphous alloy surface long before the surface may otherwise be ready for such crystallization [4.33].

4.3 Effects of Surface Contamination by Diffusion

Surface contaminant films may form by diffusion of bulk contaminants through the solid itself. An example of this type of surface contamination and the usefulness of XPS for analyzing the surface chemical composition was demonstrated for three ferrous-based amorphous alloys (metallic glasses).

Sliding friction experiments were conducted with foil specimens of Al_2O_3 in contact with amorphous alloys in vacuum at temperatures to 750 °C [4.34, 4.35]. Friction force traces resulting from such sliding were generally characterized by fluctuating behavior with evidence of stick-slip. Figure 4.30 presents the coefficients of friction as a function of sliding temperature. The Al_2O_3 pin was sputter cleaned with argon ions at room temperature. The foil specimen was also sputter cleaned with argon ions in the vacuum system and then heated from room temperature to 750 °C. Temperature effects drastically changed the friction behavior of the amorphous alloys. There was also a considerable difference in the friction measured for the three alloy compositions.

As the temperature increased from room temperature to 350 °C, the friction increased (Fig. 4.30). Why did this appreciable increase occur? Is the increase in friction associated with changes in the chemical and microstructural states of the contacting materials? Further, at 500 °C (Fig. 4.30) the friction underwent a marked decrease from that measured at 350 °C. Does surface analysis supply the answer? To answer these questions, surface and bulk analyses of the amorphous alloys were conducted.

4.3.1 Bulk Composition and Microstructure of Amorphous Alloys

Three amorphous alloy compositions were examined in this investigation. Table 4.2 lists the compositions and some of their properties. The alloys were foils (30- to 33-μm-thick ribbon) and were in the as-cast condition. To establish the exact crystalline state of the amorphous alloy surfaces, their microstructures were

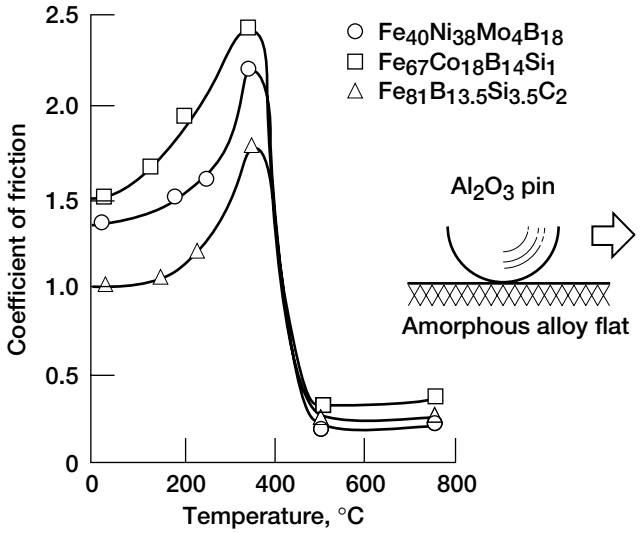

Figure 4.30.—Coefficient of friction as function of temperature for Al_2O_3 pins sliding on ferrous-base amorphous alloys (metallic glasses).

TABLE 4.2.—PROPERTIES OF METALLIC GLASSES

Nominal alloy composition, wt%	Crystallization temperature, °C	Density, g/cm^3	Hardness, GPa	Ultimate tensile strength, GPa	Bend ductility[a]
$Fe_{67}Co_{18}B_{14}Si_1$	430	7.56	10	1.5	1
$Fe_{81}B_{13.5}Si_{3.5}C_2$	480	7.3	10.3	0.7	9×10^{-3}
$Fe_{40}Ni_{38}Mo_4B_{18}$	410	8.02	10.5	1.38	1

[a] $\varepsilon = t(d - t)$, where t is ribbon thickness and d is micrometer spacing at bend fracture.

examined by transmission electron microscopy and diffraction in a microscope operating at 100 kV.

Figure 4.31 shows a typical structure of the as-received amorphous alloy foils. Amorphous alloys lack the macroscopic structural features common in crystalline metals. In the absence of macroscopic crystallinity neither grains, grain boundaries, grain orientation, nor additional phases exist. However, black spots, believed to be nuclei and/or crystallites with a size range to 4 nm, are apparent in the photomicrograph. Diffused honeycomb-shaped structures formed by segregation and clustering of transition metals and metalloids are also apparent in the photomicrograph (dark gray bands). The electron diffraction pattern for the as-received foil (Fig. 4.31) indicates that the foil was not completely amorphous but contained extremely small nuclei and/or clusters of a few nanometers in size.

Figure 4.32 shows typical examples of an amorphous alloy foil structure after heating to 350 and 430 °C for 20 min in ultrahigh vacuum. The foil structure heated to 350 °C (Fig. 4.32(a)) was similar to the as-received foil (Fig. 4.31). After

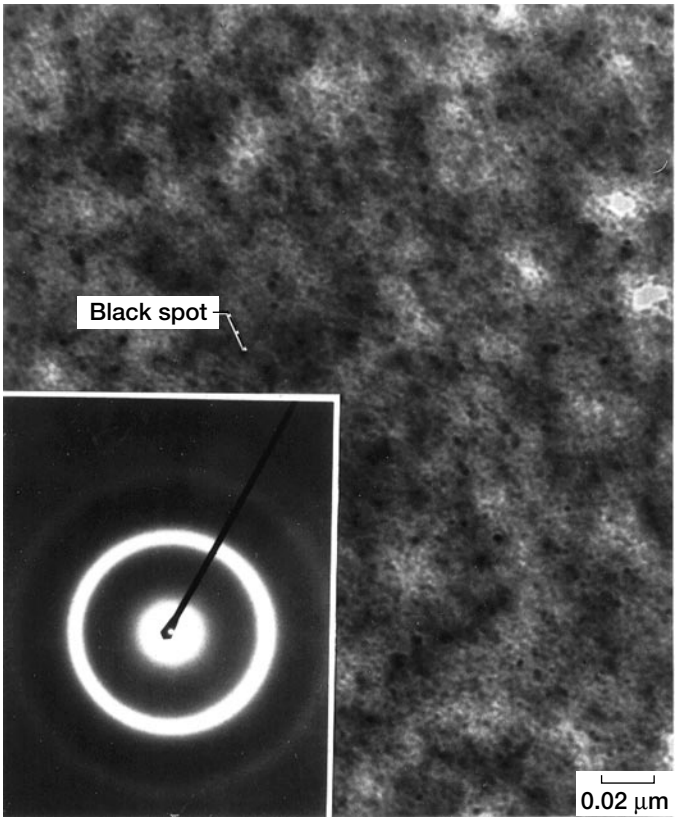

Figure 4.31.—Typical microstructure and electron diffraction pattern of an amorphous alloy ($Fe_{67}Co_{18}B_{14}Si_1$).

heating to 430 °C (Fig. 4.32(b)), the so-called crystallization temperature for this particular $Fe_{67}Co_{18}B_{14}Si_1$ foil, the black spots were slightly larger than those shown in Figs. 4.31 and 4.32(a). The diffused honeycomb-shaped structure (dark gray bands) was enriched, suggesting that the amorphous alloy structure subdivided as a result of decomposition and separation of the amorphous phase. That is, the constituents were segregating and preferential clustering occurred at this temperature. The electron diffraction pattern also indicates the presence of an extra outer ring related to clustering or crystallinity.

Figures 4.32(c) and (d) present microstructures of the same amorphous alloy heated to 500 and 750 °C. They reveal two kinds of extremely fine-grained crystals: a dark grain and a light grain. Energy-dispersive x-ray analysis (EDXA) indicated that the light grains contained about 20 times more silicon than the dark grains. The dark grains contained more iron and FeB alloy. The transmission electron diffraction patterns for both the dark and light grains contained diffraction

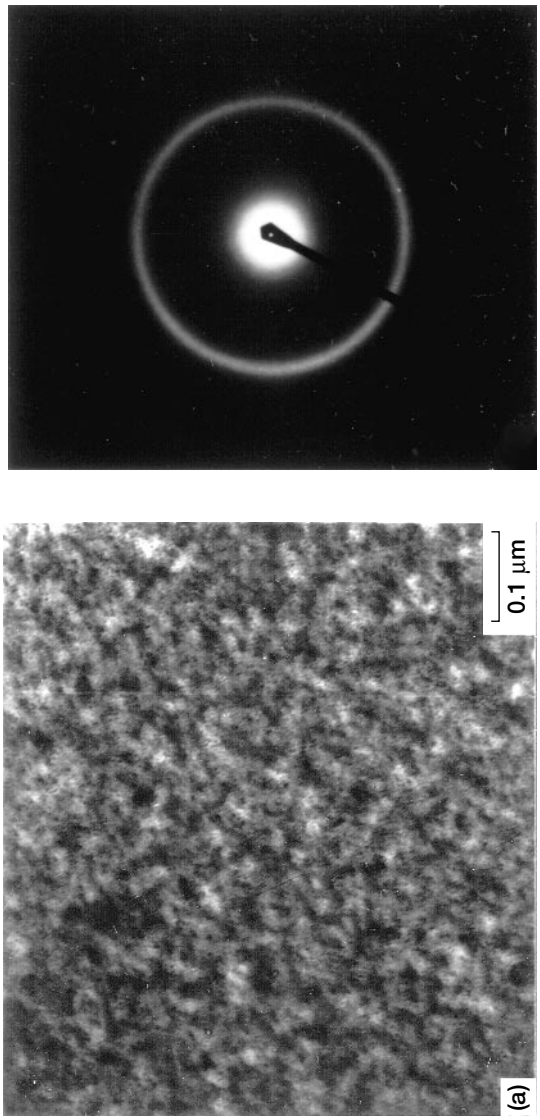

Figure 4.32.—Microstructures and electron diffraction patterns of an amorphous alloy ($Fe_{67}Co_{18}B_{14}Si_1$) heated to (a) 350 °C, (b) 430 °C, (c) 500 °C, and (d) 750 °C in vacuum (10 nPa).

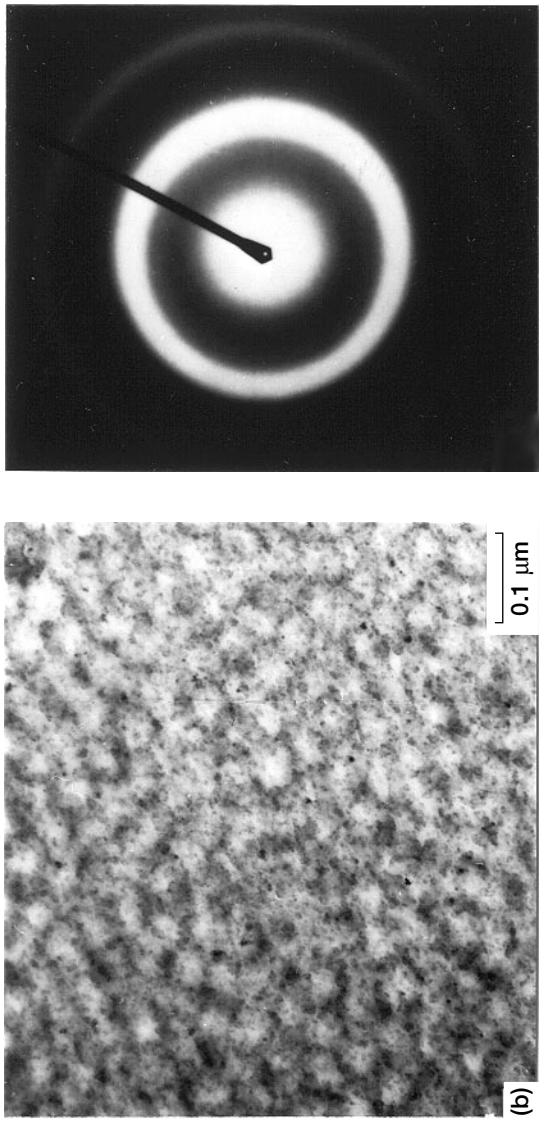

Figure 4.32.—Continued. (b) 430 °C.

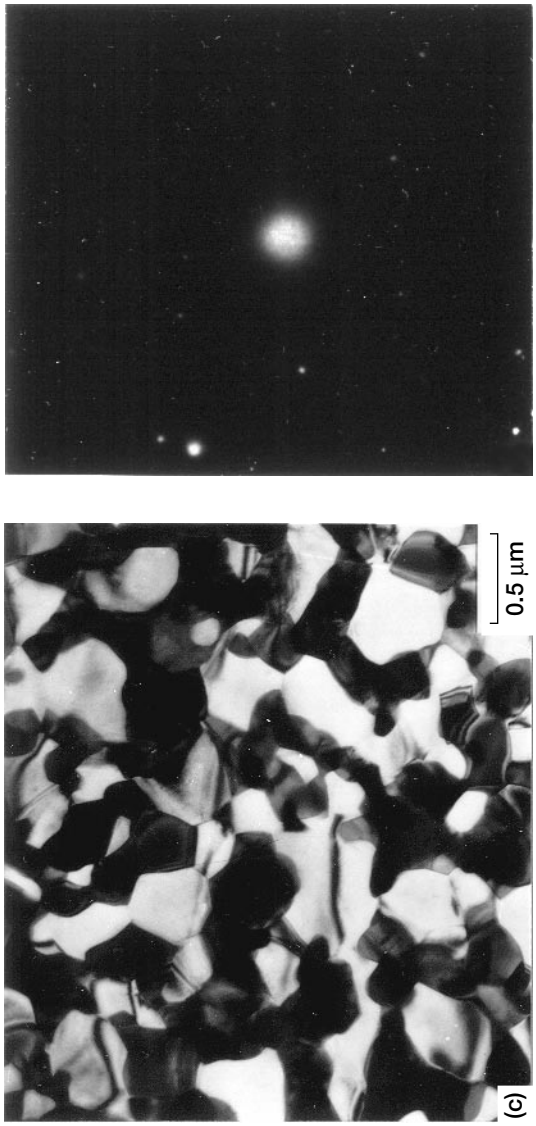

Figure 4.32.—Continued. (c) 500 °C.

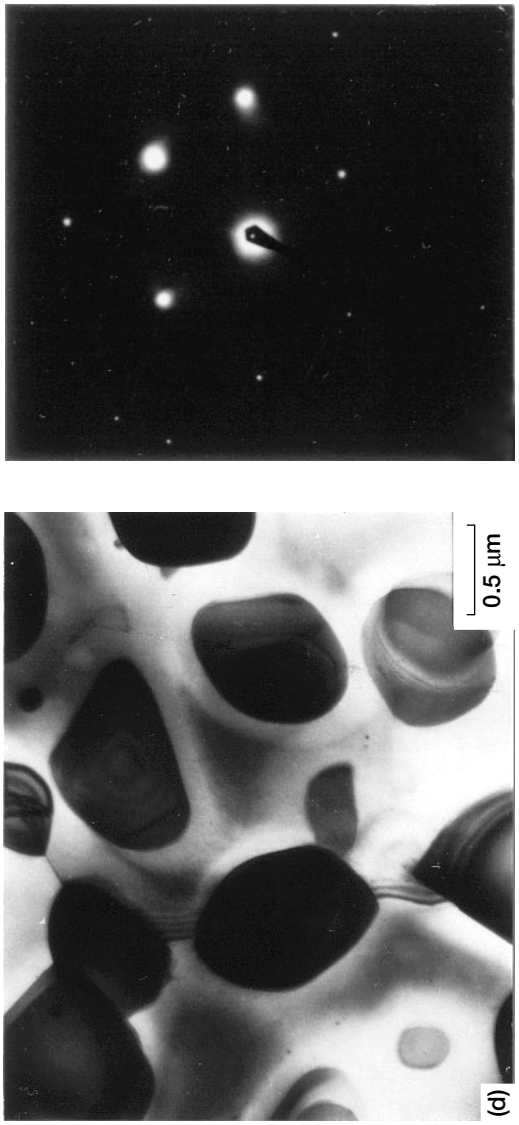

Figure 4.32.—Concluded. (d) 750 °C.

spots and Kikuchi lines indicative of single-crystal structure. The crystallized grain size was 0.7 μm at 500 °C and as large as 1.4 μm at 750 °C. Thus, the microstructure of the amorphous alloy changed discontinuously and drastically during the amorphous-to-crystalline transition. The amorphous phase separated into two crystalline phases.

4.3.2 Surface Chemistry

All XPS spectra taken from the surfaces of three as-received amorphous alloys clearly revealed adsorbed oxygen and carbon contaminants in addition to the various alloying constituents of the nominal bulk composition. Beneath this adsorbate layer there was a mixture layer comprising oxides of the alloying constituents.

Figure 4.33 presents Fe_{2p} peaks for the as-received $Fe_{67}Co_{18}B_{14}Si_1$ specimen. Before cleaning, the surface clearly contained iron oxides, such as Fe_2O_3. After the amorphous alloy surface had been argon sputter cleaned for 2 and 4 min, the Fe_{2p} lines were split asymmetrically into doublet peaks, associated with iron oxides and iron. After 60 min of argon sputter cleaning the Fe_{2p} peaks associated with iron are clearly present but the iron oxide peak is extremely small. The results after 30 min of sputtering were similar to those after 60 min.

The as-received $Fe_{67}Co_{18}B_{14}Si_1$ amorphous alloy contained the oxides of cobalt, boron, and silicon as well as iron oxides [4.36]. The oxide layers are extremely important for amorphous alloys from a tribological point of view because they are hard and tenaciously bonded to the alloying constituents. Thus, the oxide layers can provide good wear resistance, as discussed in the following section.

The XPS spectra of the surface after argon ion sputtering for 60 min contained small amounts of carbide and oxide contaminants, such as SiC and SiO_2, although the $Fe_{67}Co_{18}B_{14}Si_1$ amorphous alloy was not supposed to contain carbon and oxygen. The contaminants (i.e., oxygen and carbon) may be introduced from the environment into the bulk of the alloy and form bulk contaminants, such as carbides and oxides, in the alloy during the casting process.

Table 4.3 summarizes the argon-ion-sputter-cleaned surface conditions of the three amorphous alloy foils as analyzed by XPS. The relative concentrations of the various constituents on the surfaces were different from the nominal compositions.

Temperature effects drastically changed the surface chemistry of the amorphous alloys as analyzed by XPS—and not only above the crystallization temperature but below it as well. These changes are due to segregation and diffusion of constituents, especially of metalloids such as boron and silicon.

Figure 4.34 presents the XPS spectra for one of the ferrous-based amorphous alloys of Fig. 4.30 in the as-received condition, after sputter cleaning, and when heated to 350 and 750 °C. The XPS spectra of Fe_{2p}, Co_{2p}, B_{1s}, and Si_{2p} peaks are presented as a function of binding energy. The B_{1s} photoelectron peaks of the as-received specimen (Fig. 4.34(c)) indicate the presence of boric oxide (B_2O_3) as

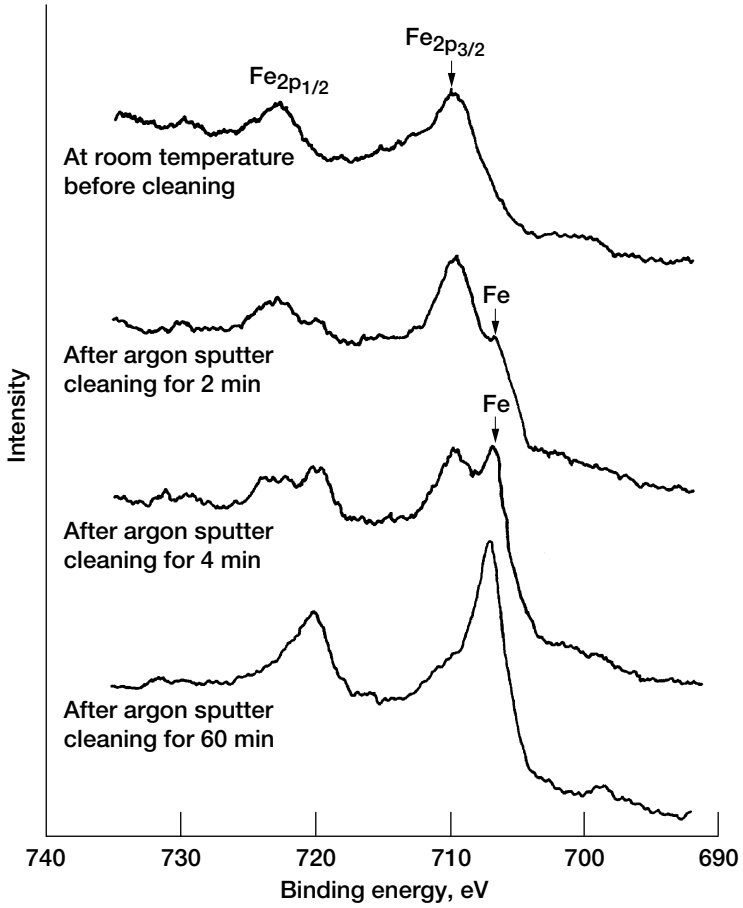

Figure 4.33.—Fe_{2p} XPS peaks on $Fe_{67}Co_{18}B_{14}Si_1$ surface.

TABLE 4.3.—COMPOSITION OF ARGON-SPUTTER-CLEANED SURFACE LAYER OF AMORPHOUS ALLOYS

Nominal bulk composition		Composition on surface, at.%[b]
wt%[a]	at.%	
$Fe_{67}Co_{18}B_{14}Si_1$	$Fe_{42}Co_{11}B_{46}Si_1$	$Fe_{49}Co_{14}B_{17}Si_6C_9O_5$
$Fe_{81}B_{13.5}Si_{3.5}C_2$	$Fe_{48}B_{42}Si_4C_6$	$Fe_{43}B_{15}Si_8C_{21}O_{14}$
$Fe_{40}Ni_{38}Mo_4B_{18}$	$Fe_{23}Ni_{21}Mo_1B_{55}$	$Fe_{18}Ni_{28}Mo_1B_{24}C_{15}O_{14}$

[a]Manufacturer's analysis.

[b]Relative concentrations of the various constituents were determined by using peak area sensitivity factors.

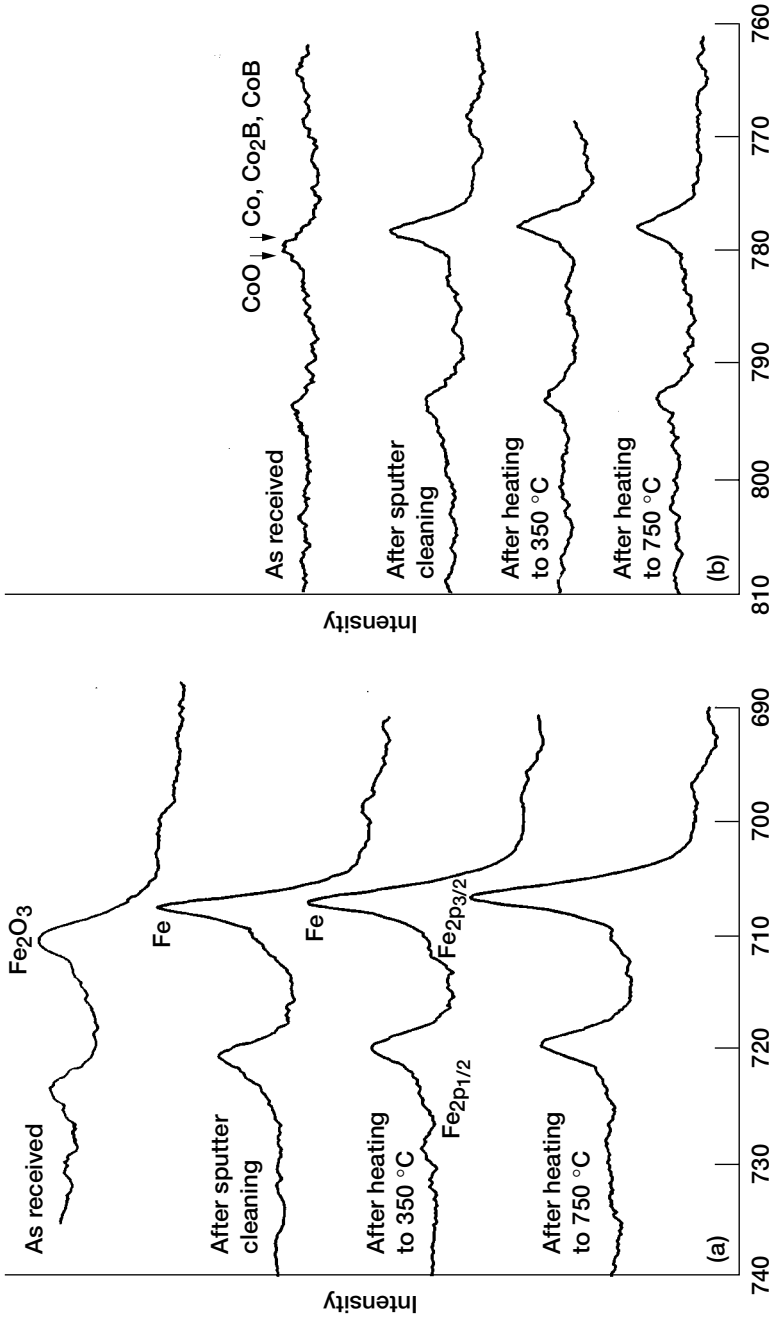

Figure 4.34.—Representative (a) Fe_{2p}, (b) Co_{2p}, (c) B_{1s}, and (d) Si_{2p} XPS peaks on $Fe_{67}Co_{18}B_{14}Si_1$ surface.

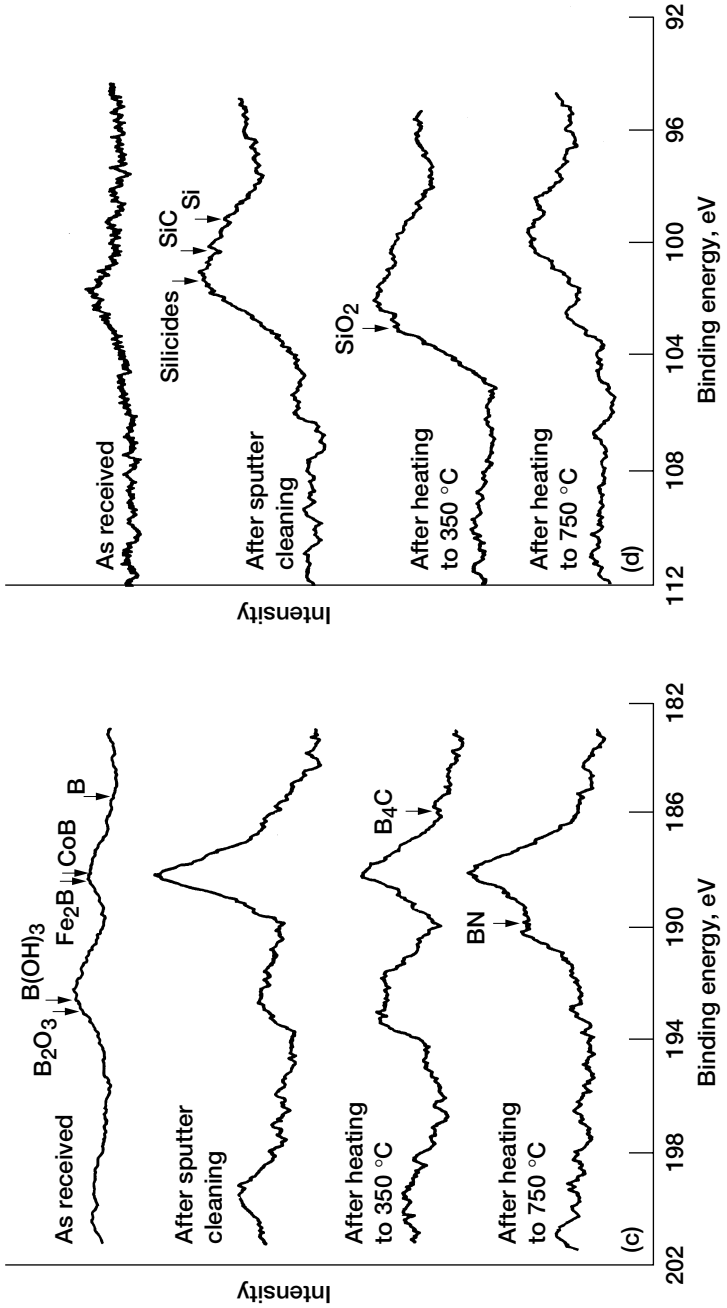

Figure 4.34.—Concluded. (c) B_{1s}. (d) Si_{2p}.

TABLE 4.4.—COMPOSITION OF SURFACE OF AMORPHOUS ALLOYS

Alloy composition	Surface			
	As received	Argon sputter cleaned	Heated to 350 °C	Heated to 750 °C
$Fe_{67}Co_{18}B_{14}Si_{1}$	Oxides of Fe, Co, B, Si, and C Adsorbed film of oxygen and carbon	Alloy Small amount of oxides and carbides	Alloy Boric oxides and silicon oxides migrated from bulk Small amount of carbides	Alloy Boron nitride migrated from bulk Very small amount of boric oxides and silicon oxides
$Fe_{81}B_{13.5}Si_{3.5}C_{2}$	Oxides of Fe, B, Si, and C Adsorbed film of oxygen and carbon	Alloy Small amount of oxides and carbides	Alloy Boric oxides and silicon oxides migrated from bulk Small amount of carbides	Alloy Boron nitride migrated from bulk Very small amount of boric oxides and silicon oxides
$Fe_{40}Ni_{38}Mo_{4}B_{18}$	Oxides of Fe, B, Ni, Mo, and C Adsorbed film of oxygen and carbon	Alloy Small amount of oxides and carbides	Alloy Boric oxides migrated from bulk Small amount of carbides	Alloy Boron nitride migrated from bulk Very small amount of boric oxides

well as Fe_2B and CoB. After argon sputter cleaning large peaks for boron and its alloys, as well as small B_2O_3 peaks, were present. After heating to 350 °C the alloy surface was again clearly contaminated with B_2O_3 and at 750 °C with BN that had migrated from its bulk. The surface heated to 500 °C was also contaminated with BN and was the same as the surface heated to 750 °C.

The Si_{2p} photoelectron peaks of the as-received surface (Fig. 4.34(d)) reveal silicides. Even the spectrum of the argon-sputter-cleaned surface reveals silicides as well as silicon dioxide (SiO_2) on the surface. After heating to 350 °C the alloy surface was contaminated with SiO_2 that had migrated from its bulk. After heating to 750 °C the alloy had a smaller amount of SiO_2 on its surface than at 350 °C.

The Fe_{2p} photoelectron peaks of the $Fe_{67}Co_{18}B_{14}Si_1$ heated to 350 and 750 °C (Fig. 4.34(a)) are almost the same as those for the argon-sputter-cleaned surface shown in Fig. 4.33.

The Co_{2p} photoelectron peaks of the as-received $Fe_{67}Co_{18}B_{14}Si_1$ (Fig. 4.34(b)) indicate cobalt oxide (CoO). The spectra for the surfaces that had been argon sputter cleaned and heated to 350 and 750 °C reveal cobalt and its alloy peaks. The cobalt peak is negligible.

Table 4.4 summarizes the surface conditions for the amorphous alloys as analyzed by XPS. Generally, the surfaces of the as-received alloys had a layer of oxides of the alloying elements as well as a simple adsorbed film of oxygen and carbon. The argon-ion-sputter-cleaned surfaces contained the alloying elements and small amounts of oxides and carbides. In addition to nominal element constituents the surfaces heated to 350 °C contained boric and silicon oxides (on $Fe_{67}Co_{18}B_{14}Si_1$ and $Fe_{81}B_{13.5}Si_{3.5}C_2$) and boric oxides (on $Fe_{40}Ni_{38}Mo_4B_{18}$), as well as small amounts of carbides that had segregated and migrated from the bulk. The surfaces heated to 750 °C contained BN that had also migrated from the bulk, as well as small amounts of oxides.

4.3.3 Frictional Response to Thermal and Chemical Changes

The increase in coefficient of friction with increasing temperature from room to 350 °C shown in Fig. 4.30 is associated with changes in the alloys' thermal, chemical, and microstructural states. First, the increase in friction is related to an increase in the adhesion resulting from the segregation of oxides, such as boric oxides and silicon oxides, to the alloy surface, as described earlier. The removal of adsorbed contaminants by sliding and the segregation of the oxides increase the adhesion strength and hence the friction.

Second, as the temperature is raised, the materials in contact soften and accordingly the total contact area increases. Thus, the enhanced strength of the interfacial bonds and the increased real area of contact are the main causes of the observed friction behavior at temperatures to 350 °C in Fig. 4.30.

The rapid decrease in friction in Fig. 4.30 between 350 and 500 °C can be attributed to the complete transformation of the alloys from the amorphous to the

crystalline state between 410 and 480 °C. After this transformation BN, a solid lubricant, diffused to the alloy surfaces and brought about the friction reduction observed in Fig. 4.30. Thus, the marked reduction in friction at 500 and 750 °C in Fig. 4.30 is related to the presence of BN on the alloy surfaces and the reduction in the amount of surface oxides, as typically indicated at 750 °C in Fig. 4.34.

In situ examination of the surface chemistry in the heating stage gives valuable information on the behavior of surface segregation and decomposition. The segregation and migration of compounds, such as boric oxide and nitride, influence the friction behavior of amorphous alloys, as shown in Fig. 4.30.

4.4 Chemical Changes With Selective Thermal Evaporation

Increasing the surface temperature of a ceramic material or metal tends to promote surface chemical reactions and to volatilize some element, as described in Chapter 2. These chemical reactions cause products, such as graphite, to appear on the surface [4.37] and thus can alter adhesion and friction [4.38, 4.39].

4.4.1 Silicon Carbide

SiC-SiC couples.—Figure 4.35 presents the average pull-off forces for SiC {0001} surfaces in contact with a sintered polycrystalline SiC pin as a function of temperature in a vacuum [4.39]. The average pull-off force and the maximum and minimum measured pull-off forces were obtained from seven or more measurements.

Figure 4.36 presents the coefficients of static and dynamic friction for the SiC {0001} surfaces in contact with sintered polycrystalline SiC pins as a function of temperature in a vacuum. The average coefficient of friction and the maximum and minimum measured coefficients of friction were obtained from five or more measurements in this case. Comparing Figs. 4.35 and 4.36 shows that the static and dynamic friction characteristics were the same as those for adhesion. Adhesion and friction generally remained low to 300 °C but increased rapidly between 300 and 400 °C. Adhesion and friction decreased slightly at 600 °C but remained relatively high between 400 and 700 °C. Above 800 °C adhesion and friction decreased rapidly.

Figure 4.37 presents the C_{1s} and Si_{2p} XPS spectra obtained from narrow scans on the single-crystal SiC surface for preheating temperatures to 1500 °C. The as-received crystal (after bakeout) was preheated at various temperatures in a 10-nPa vacuum. Preheating temperatures given in Fig. 4.37 are the highest temperature to which each crystal had been heated. All the XPS spectra were taken at room temperature after bakeout and preheating. The Si_{2p} photoelectron peak energies associated with SiC at the various temperatures underwent a gradual

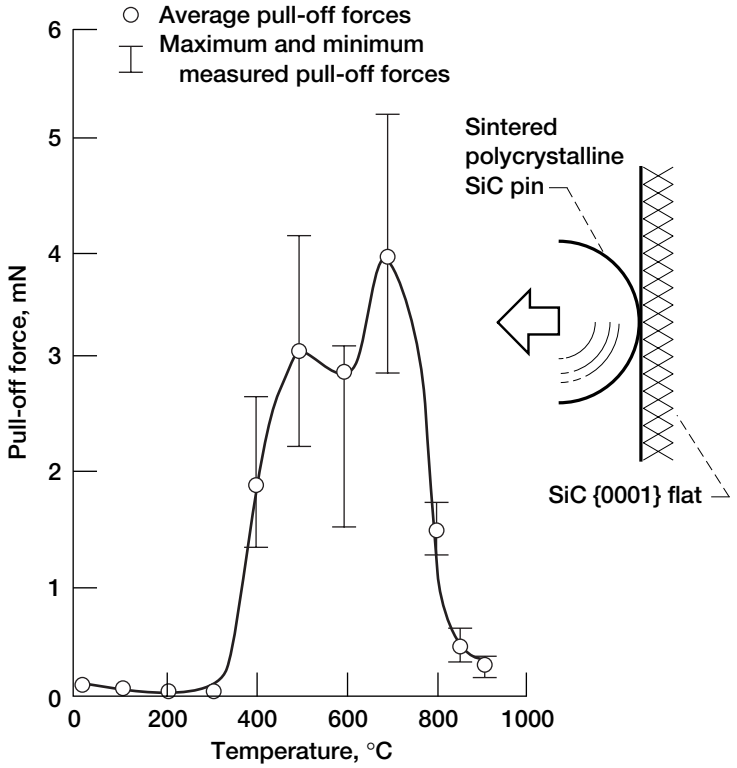

Figure 4.35.—Pull-off force (adhesion) as function of temperature for SiC {0001} flat surfaces in sliding contact with sintered polycrystalline SiC pins in vacuum.

change from 16.06 attojoules (aJ) (100.4 eV) (at 250 °C bakeout temperature) to 16.0 aJ (100.0 eV) (at 1500 °C preheating temperature). The vertical heights, peak to baseline, of the Si_{2p} peaks in the spectra were lowest at the bakeout temperature and highest at 800 °C. They were nearly the same at 400 and 600 °C. But above 800 °C the Si_{2p} for SiC decreased gradually.

The C_{1s} photoelectron emission lines for SiC were split asymmetrically into doublet peaks (Fig. 4.37), showing a significant influence of temperature on the SiC surface. Three spectral features, dependent on the chemical nature of the specimen, can be observed: (1) two kinds of doublet peaks, (2) a change in the vertical height of the peaks, and (3) a shift of peaks.

The doublet peaks were due to distinguishable kinds of carbon: (1) a carbon contamination peak and a carbide peak at room temperature and (2) graphite and carbide peaks at 400 to 1500 °C. For the XPS spectra of the as-received specimens (Fig. 4.37(a)) the carbon contamination peak was higher than the carbide peak. At 250 °C (Fig. 4.37(b)) the primary peaks were adsorbed amorphous carbon

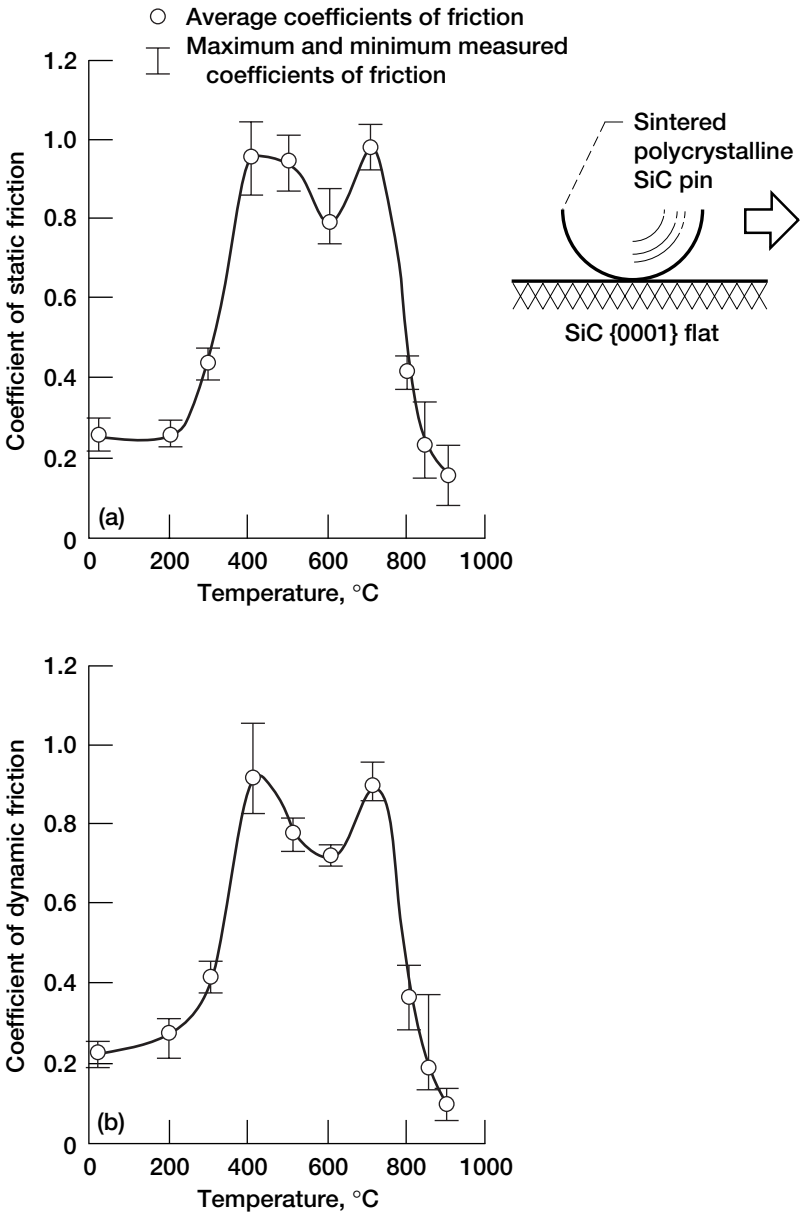

Figure 4.36.—Coefficients of static (a) and dynamic (b) friction as functions of temperature for SiC {0001} flat surfaces in sliding contact with sintered polycrystalline SiC pins in vacuum.

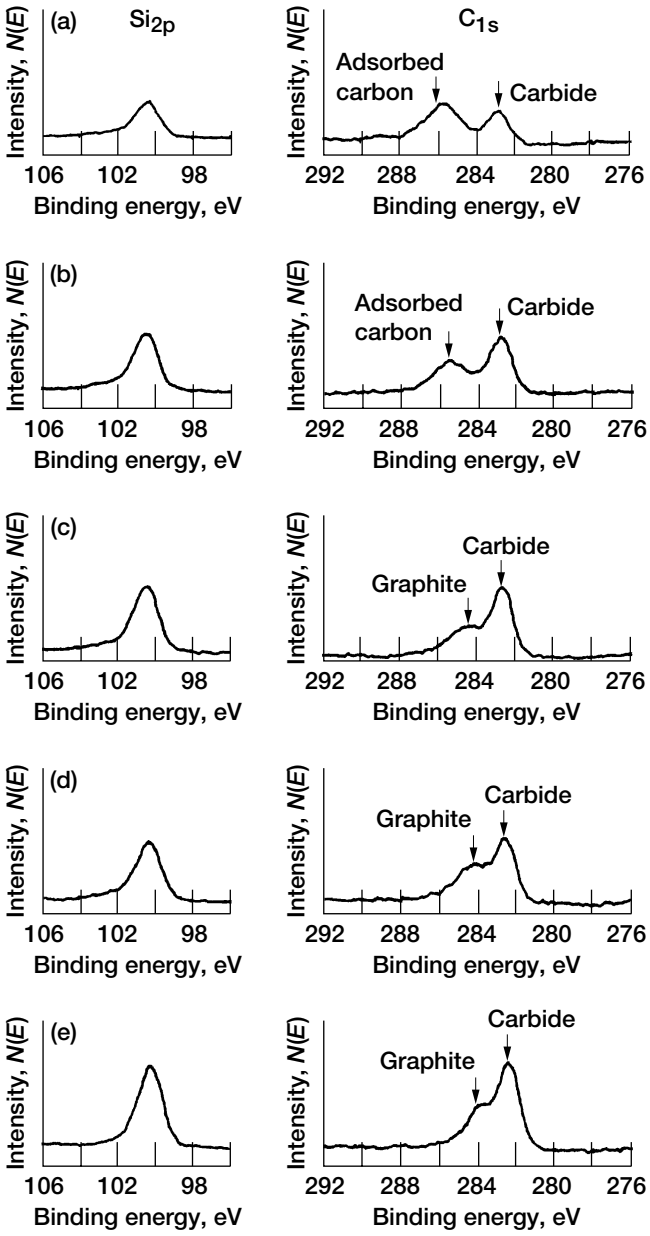

Figure 4.37.—Representative Si_{2p} and C_{1s} peaks on SiC {0001} surface preheated at various temperatures. (a) Room temperature. (b) 250 °C. (c) 400 °C. (d) 600 °C. (e) 800 °C. (f) 900 °C. (g) 1000 °C. (h) 1500 °C.

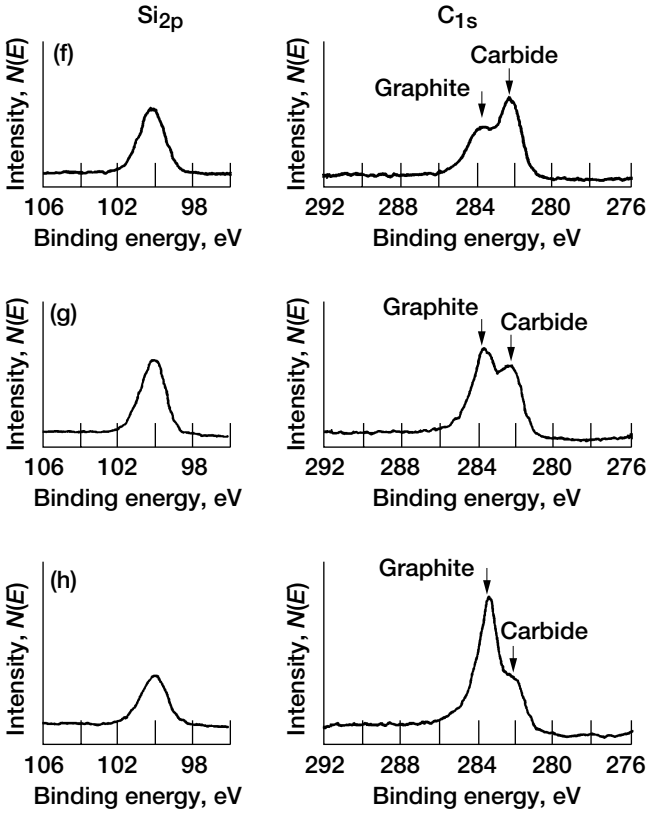

Figure 4.37.—Concluded. (f) 900 °C. (g) 1000 °C. (h) 1500 °C.

contamination and carbide, and the contaminant peak was lower than the carbide peak. At 400 °C and above (Figs. 4.37(c) to (h)) the carbon contamination peak disappeared from the spectrum and was replaced by the graphite and carbide peaks. Both the graphite and the carbide peaks increased with an increase in preheating temperature. A high carbide peak was distinguished at 800 °C (Fig. 4.37(e)).

AES analysis of an SiC surface preheated at 800 °C indicated that the AES spectrum was the same as that obtained for an argon-sputter-cleaned surface and that the spectrum included carbide-type carbon as well as a silicon peak on the surface. The AES spectrum indicated that the surface was pure SiC. But XPS analysis, which can provide more detailed chemical information than AES, clearly indicated the presence of graphite on the SiC surface preheated at 800 °C. At 900 °C (Fig. 4.37(f)) the carbide peak was lower and the graphite peak higher than at 800 °C. Nevertheless, the carbide peak remained higher than the graphite peak until 1000 °C (Fig. 4.37(g)). At 1500 °C (Fig. 4.37(h)) the carbide peak became extremely low and the graphite peak extremely high.

AES analysis of an SiC surface preheated at 1500 °C indicated that the silicon AES peak had almost disappeared and that the carbon peak was only the graphite form. However, XPS analysis of the same surface indicated evidence for silicon and carbide as well as graphite. This difference can be accounted for by the fact that XPS analyzes to greater depths and is more sensitive to the presence of silicon than is AES.

The narrow scans in Fig. 4.37 also show the shift of C_{1s} and Si_{2p} peaks on the SiC surface. All the C_{1s} of adsorbed carbon, carbide, and graphite and the Si_{2p} of SiC shifted toward lower binding energy with increasing temperature. For the carbon contamination peak C_{1s} at 45.70 aJ (285.6 eV) the shift was small (0.05 aJ to 0.06 aJ), almost the same as the instrument error (±0.05 aJ). The carbide peak shifted from 45.23 aJ (282.7 eV) at room temperature to 45.15 aJ (282.2 eV) at 1500 °C, and the graphite peak from 45.52 aJ (284.5 eV) at 400 °C to 45.38 aJ (283.6 eV) at 1500 °C. The Si_{2p} peak shifted from 16.08 aJ (100.5 eV) on the as-received surface to 16.02 aJ (100.0 eV) at 1500 °C.

Figure 4.38 presents the XPS heights of the high-resolution Si_{2p}, C_{1s}, and O_{1s} spectral peaks on single-crystal SiC surfaces as a function of a preheating temperature to 1500 °C. An adsorbed carbon contaminant on the as-received surface at room temperature is evident as well as a minute amount of oxygen contaminant. The concentration of silicon carbide Si_{2p} and C_{1s} on the single-crystal SiC surface (Fig. 4.38(a)) increased with increasing temperature from 23 to 800 °C but decreased above 800 °C. Large Si_{2p} and C_{1s} peaks associated with SiC were at maximum intensity at 800 °C. The peak heights of silicon dioxide Si_{2p} and O_{1s} (Fig. 4.38(b)) remained relatively low at 23 to 1500 °C and were almost negligible at 800 to 1500 °C. The adsorbed carbon contaminant C_{1s} peak height (Fig. 4.38(c)) decreased with increasing temperature and was negligible above 400 °C. Also, the graphite C_{1s} peak was absent from room temperature to 250 °C and remained low from 400 to 800 °C but increased rapidly from 900 to 1500 °C. Because the graphite C_{1s} peak on the SiC surface was extremely high at 1000 °C and above, the SiC surface must have been covered with a graphite layer above 1000 °C.

Comparing Fig. 4.38 with Figs. 4.35 and 4.36 shows that the low adhesion and friction between room temperature and 300 °C were caused by carbon contaminants on the SiC flat surface. The rapid increase in adhesion and friction between 300 and 400 °C can be attributed to the absence of adsorbed contaminants. The high adhesion and friction between 400 and 800 °C were primarily related to the absence of adsorbed contaminants and to a small amount of SiO_2 on the SiC surface. The somewhat low adhesion and friction at 600 °C were probably caused by the known α-SiO_2-to-β-SiO_2 transition of a small amount of SiO_2 at about 583 °C [4.40] and by changes in the amount of SiO_2 on the single-crystal SiC surface. The somewhat low adhesion and friction at 600 °C were related to the slight increase in SiO_2. The silicon dioxide Si_{2p} and O_{1s} peak heights obtained from the SiC surface at 800 °C and above were extremely small (Fig. 4.38).

The low adhesion and friction above 800 °C correlated with the graphitization of the SiC surface. Note that using both XPS and AES to study the SiC surface

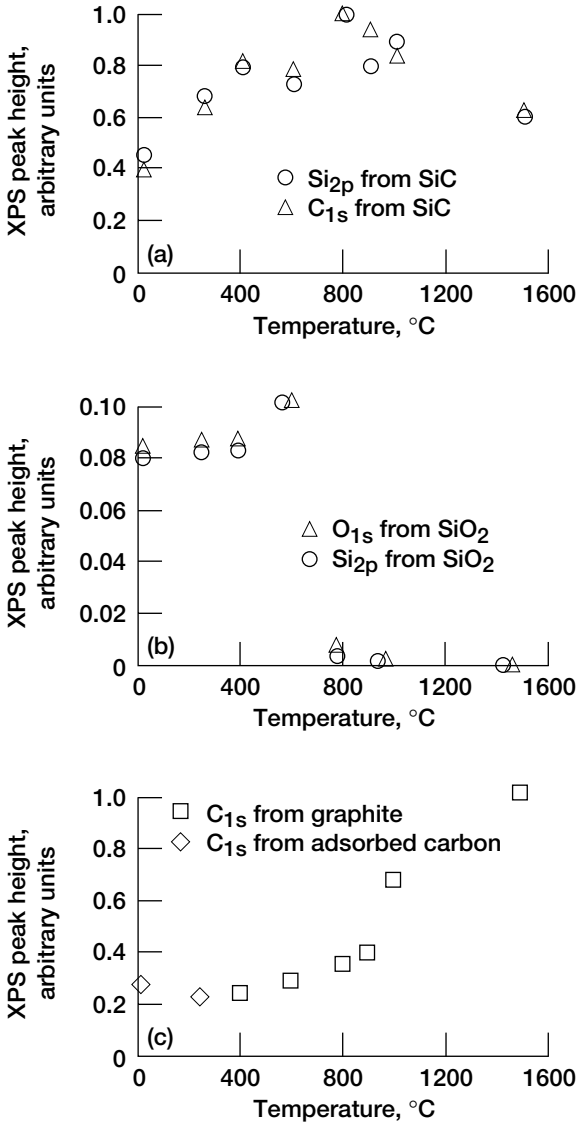

Figure 4.38.—Si_{2p}, C_{1s}, and O_{1s} XPS peak heights on single-crystal SiC surface preheated at various temperatures. (a) Si_{2p} and C_{1s} peak heights from SiC. (b) Si_{2p} and O_{1s} peak heights from SiO_2. (c) C_{1s} peak heights from graphite and adsorbed carbon.

revealed that the low adhesion and friction above 800 °C (Figs. 4.35 and 4.36) resulted from graphitization of the SiC surface by selective thermal evaporation of silicon with heating. The XPS and AES analyses complemented each other in this determination.

Iron-SiC couples.—The principal contaminants (as determined by XPS) on the as-received, sintered polycrystalline SiC surface at room temperature were adsorbed carbon and oxygen, residual graphite, and SiO_2 (Fig. 4.39). The residual graphite was generated during fabrication in an argon atmosphere. The adsorbed carbon contaminants disappeared on heating to 400 °C. Above 400 °C primarily graphite and SiO_2 appeared on the SiC surface. The amount of SiO_2 decreased rapidly from 600 to 800 °C (Figs. 4.39(a) and (c)). At 800 °C the silicon carbide Si_{2p} and C_{1s} peaks were at maximum intensity. Above 800 °C the graphite concentration increased rapidly, whereas the SiC concentration decreased rapidly, in intensity (Fig. 4.39(b)). The SiC surface graphitized predominantly at 1000 to 1200 °C.

Temperature distinctly influenced the Si_{2p}, C_{1s}, and O_{1s} concentrations on sintered, polycrystalline SiC surfaces. Figure 4.40 shows the heights of the Si_{2p} peaks (SiC and SiO_2), the C_{1s} peaks (adsorbed carbon contaminant, graphite, and SiC), and the O_{1s} peaks (adsorbed oxygen contaminant and SiO_2) as a function of preheating temperature. Over the entire temperature range (room to 1200 °C) the trend of Si_{2p} concentration from SiC was similar to that of C_{1s} from SiC (Fig. 4.40(a)). The silicon carbide Si_{2p} and C_{1s} peak heights increased linearly to 800 °C and then decreased above 800 °C. The carbon contaminant C_{1s} peak height decreased rapidly to 400 °C (Fig. 4.40(b)). Whereas the graphite C_{1s} peak was absent on as-received, single-crystal SiC, it was present on as-received, sintered, polycrystalline SiC and is thus a distinguishing feature of that surface. The graphite C_{1s} peak height (Fig. 4.40(b)) was relatively constant to 400 °C but increased above 400 °C, becoming large at 1000 and 1200 °C. In other words, the SiC surface is covered with a graphite layer.

The trends of the silicon dioxide O_{1s} and Si_{2p} peak heights were similar (Fig. 4.40(c)), increasing to 600 °C and then decreasing rapidly. Three times more SiO_2 was present on the polycrystalline SiC than on the single-crystal SiC.

Figure 4.41 presents the coefficients of friction for sintered polycrystalline SiC flat surfaces in sliding contact with an iron pin as a function of sliding temperature. The iron pin was sputter cleaned with argon ions. The as-received SiC was baked out in the vacuum system and then heated to the sliding temperature before the friction experiment began. The low coefficients of friction below 250 °C can be associated with both carbon and graphite contaminants on the as-received specimen. The rapid increase in friction at 400 °C can be attributed to the absence of carbon contaminants, increased SiO_2, and increased plastic flow causing junction growth in the contact zone. The rapid decrease in friction above 800 °C correlated with SiC surface graphitization, similar to what occurred with single-crystal SiC.

Figure 4.42 presents the coefficients of friction for SiC {0001} surfaces in contact with an iron pin as a function of sliding temperature. The iron pin was

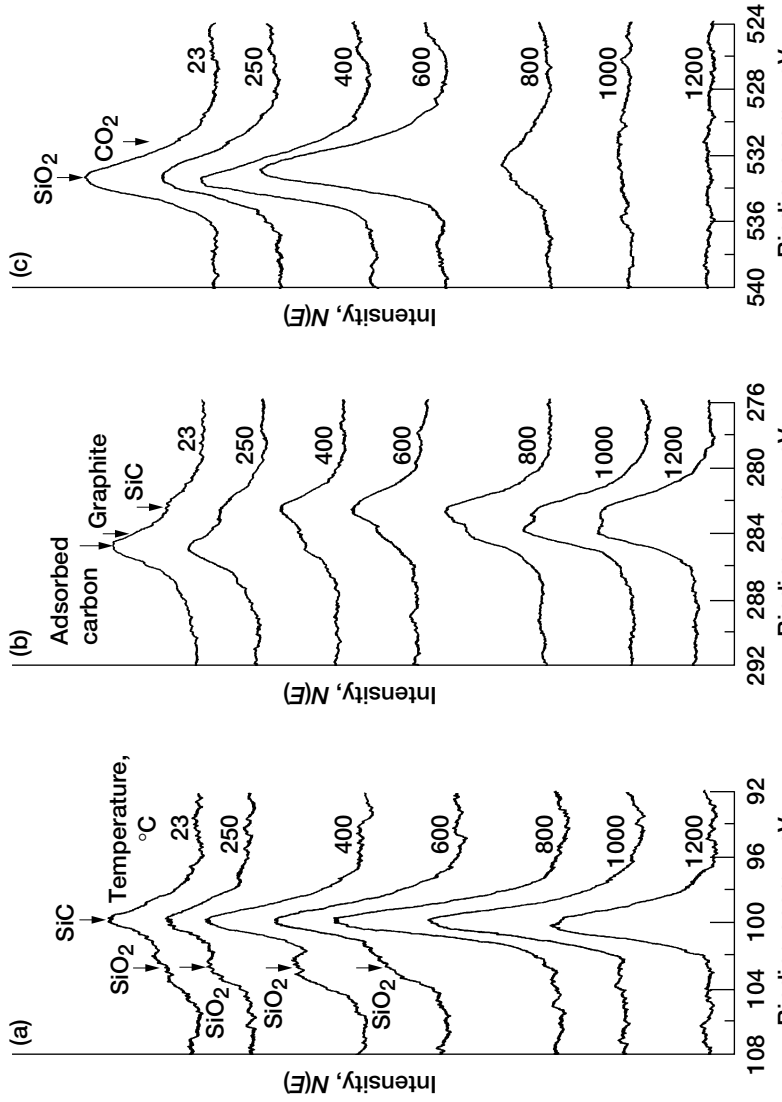

Figure 4.39.—Representative (a) Si_{2p}, (b) C_{1s}, and (c) O_{1s} peaks on sintered polycrystalline SiC surface preheated at various temperatures.

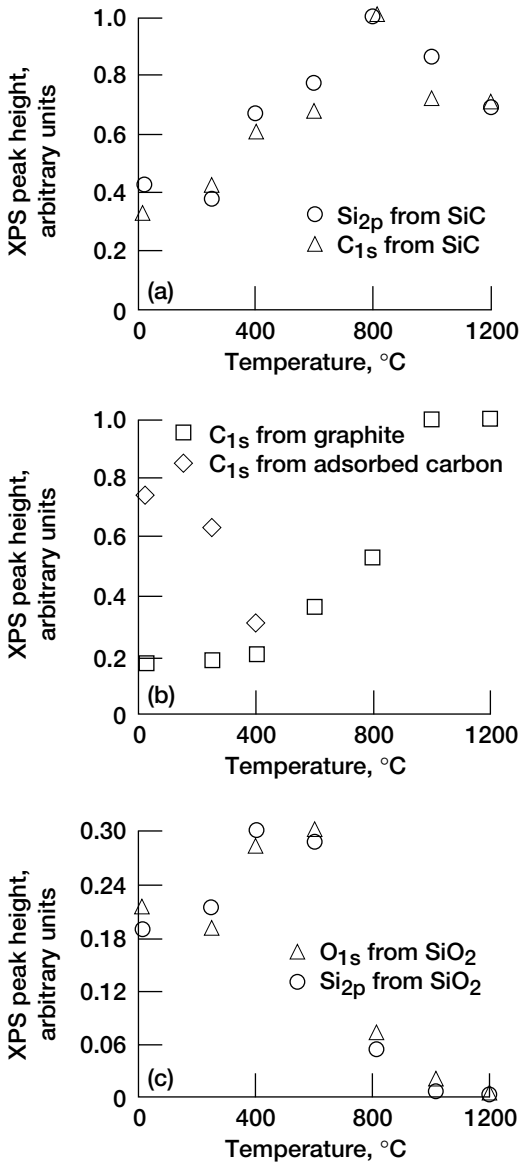

Figure 4.40.—Si_{2p}, C_{1s}, and O_{1s} XPS peak heights on sintered polycrystalline SiC surface preheated at various temperatures. (a) Si_{2p} and C_{1s} peak heights from SiC. (b) C_{1s} peak heights from graphite and adsorbed carbon. (c) Si_{2p} and O_{1s} peak heights from SiO_2.

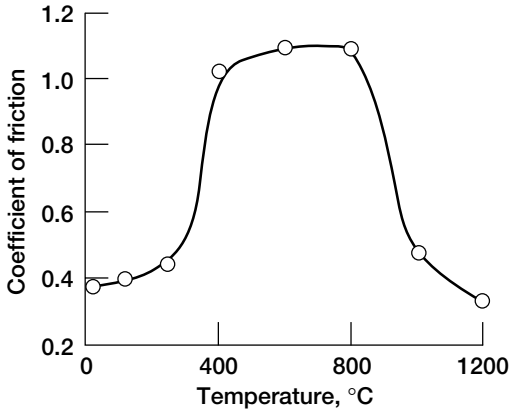

Figure 4.41.—Coefficient of friction as function of temperature for sintered polycrystalline SiC surface sliding against iron pin that was argon ion sputter cleaned before experiments. Normal load, 0.1 to 0.2 N; vacuum, 30 nPa.

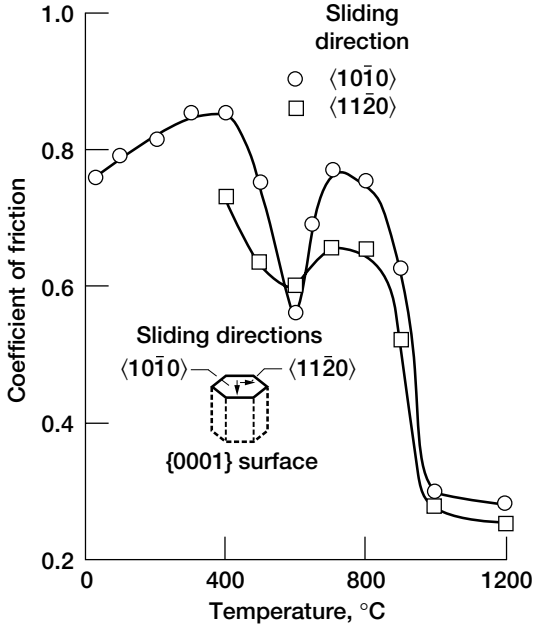

Figure 4.42.—Coefficient of friction as function of temperature for SiC {0001} surface sliding against iron pin that was argon ion sputter cleaned before experiments. Normal load, 0.2 N; vacuum, 10 nPa.

sputter-cleaned with argon ions. The as-received SiC was baked out in the vacuum system and then heated to the sliding temperature before the friction experiment began. The coefficient of friction increased slightly below 400 °C and then decreased from 400 to 600 °C because carbon and oxygen contaminants were gradually removed from the surface. The coefficient of friction increased from 600 to 800 °C because both adhesion and plastic flow increased in the contact area. Above 800 °C the coefficient of friction decreased rapidly in correlation with graphitization of the single-crystal SiC surface. The coefficients of friction on single-crystal and sintered polycrystalline SiC surfaces at high temperatures were nearly the same as those on pyrolytic graphite in sliding contact with iron in a vacuum [4.41].

Heating single-crystal SiC from 800 to 1500 °C graphitized the SiC surface. XPS analysis demonstrated that silicon segregated and evaporated in the SiC surficial region and that the remaining carbon reconstructed at the SiC surface. After the SiC specimen had cooled to room temperature, sliding friction experiments from room temperature to 1200 °C in vacuum were conducted on the graphitized surface. Figure 4.43 presents the friction properties. The SiC specimens preheated to 1500 °C produced coefficients of friction lower, by one-half, than those for the surfaces cleaned by argon ion sputtering. The marked difference in friction between graphitized and nongraphitized surfaces was observed even in air [4.42]. Thus, with heating the SiC generates its own solid-lubricant surface films in the form of graphite.

Mechanisms of SiC graphitization.—Meyer and Loyen [4.43] conducted ellipsometric measurements above 1200 °C with two different SiC crystal {0001} faces, one consisting of silicon atoms {0001} and the other consisting of carbon atoms {0001}. In 1 hr of heating at 1300 °C the carbon (graphite) layer on the

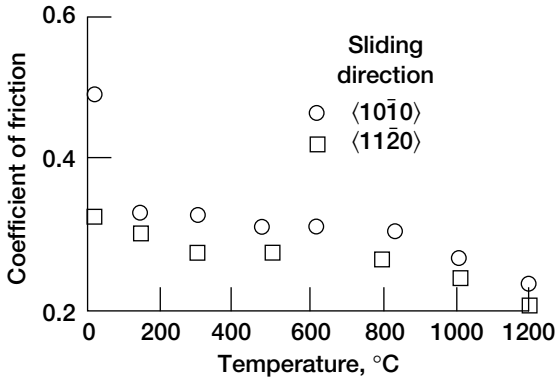

Figure 4.43.—Coefficient of friction as function of temperature and crystallographic orientation for single-crystal SiC {0001} surface preheated to 1500 °C sliding against iron pin. Normal load, 0.2 N; vacuum, 10 nPa.

carbon face grew to about 100 nm, whereas the layer on the silicon face did not grow thicker than 10 nm even with longer heating. Figure 4.44 presents a typically complete elemental depth profile for an SiC surface preheated to 1500 °C as a function of sputtering time. The graphite C_{1s} peak decreased rapidly in the first 30 min of sputtering and then decreased gradually to about 18 hr. After 18 hr the graphite peak did not change much with sputtering time. On the other hand, the Si_{2p} and carbide C_{1s} peaks increased gradually to 20 hr. The SiC {0001} surfaces consisted of both silicon and carbon atoms because etching the SiC surface in molten salt ($1NaF + 2KCO_3$) gave both a smooth surface for the silicon face and a rough one for the carbon face. Figure 4.45 shows that the apparent thickness of the intermediate layer (a mixture of graphite and SiC) produced by heating above 1200 °C for 1 hr was about 100 nm (1000 Å), equivalent to the depth of a layer sputter etched for about 18 hr.

The graphitization behavior in the outermost surficial layer can be as follows. The AES analysis depth is 1 nm or less, and an elemental concentration as low as 0.1% of a monolayer can be detected and identified. The XPS analysis depth is 2 nm or less, and the ultimate sensitivity is sufficient to allow fractions of a monolayer to be detected and identified. Therefore, Meyer and Loyen [4.43] concluded the outermost SiC surficial layer, consisting mostly of graphite with little silicon, to be 2 nm. This estimation is consistent with the proposition of Van Bommel et al. [4.44]; that is, the collapse of the carbon in two or three successive SiC layers after

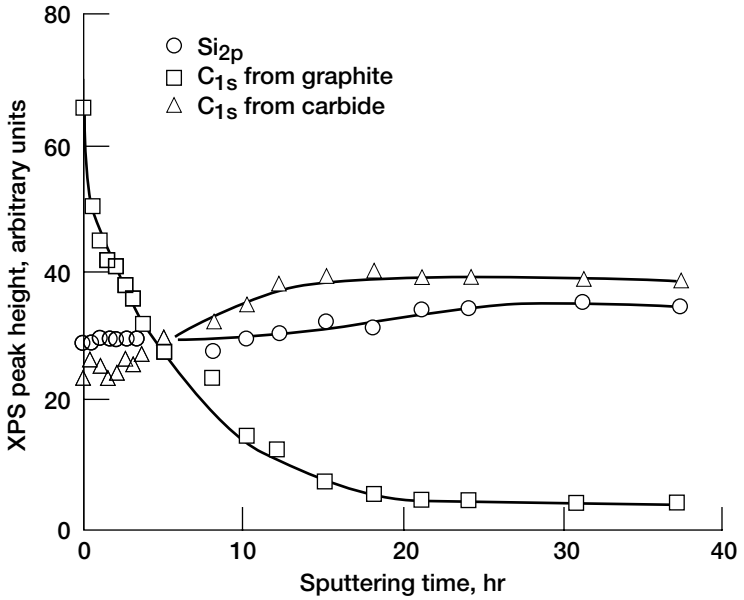

Figure 4.44.—Elemental depth profiles of SiC {0001} surface preheated to 1500 °C for 1 hr.

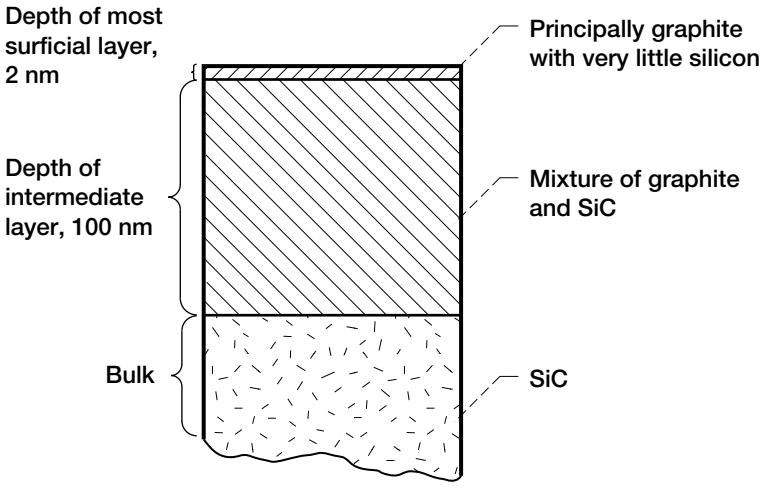

Figure 4.45.—Surface condition of SiC after heating above 1200 °C.

the silicon has evaporated from two or three successive SiC layers (Fig. 4.46) is the most probable mechanism in the initial stages of SiC basal plane graphitization.

4.4.2 Diamondlike Carbon Coatings

Diamondlike carbons (DLC's), such as amorphous hydrogenated carbon (a-C:H), can be considered as metastable carbons produced as thin coatings with a broad range of structures (primarily amorphous with variable sp^2/sp^3 carbon bonding ratio) and compositions (variable hydrogen concentration). DLC converts to graphite or other nondiamond carbon at lower temperatures than diamond [4.45]. An initial transformation has been observed as low as 250 °C. The transformation usually occurs at 400 °C and proceeds by loss of hydrogen and subsequent graphitization. Maximum long-term use temperature for DLC ranges from 250 to 300 °C.

Figure 4.47 presents the hydrogen concentration in as-deposited and rapidly thermal annealed DLC films [4.46]. The DLC films were deposited by a direct ion beam deposition technique using methane ions. Thermally annealed DLC films were prepared by rapidly heating the as-deposited DLC films at 300 deg C/s in a nitrogen atmosphere for 2 min at various temperatures to 1000 °C.

The as-deposited DLC film contained 30% hydrogen, as did the rapid thermally annealed DLC films when the annealing temperature was below 500 °C. Therefore, the chemical composition of DLC does not change with temperature below 500 °C. The hydrogen concentration decreased linearly with annealing temperature between 500 and 900 °C to 5% at 900 °C. Several researchers have reported that heat treating hydrocarbon films, which leads to hydrogen evolution, causes structural changes between 400 and 600 °C [4.47, 4.48].

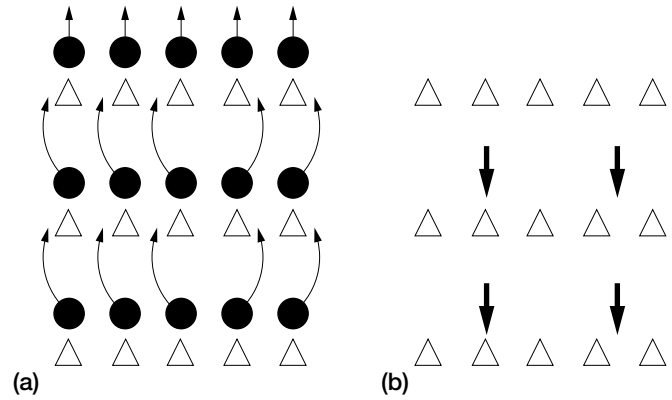

Figure 4.46.—Graphitization of SiC surface. (a) Evaporation of silicon. (b) Collapse of carbon.

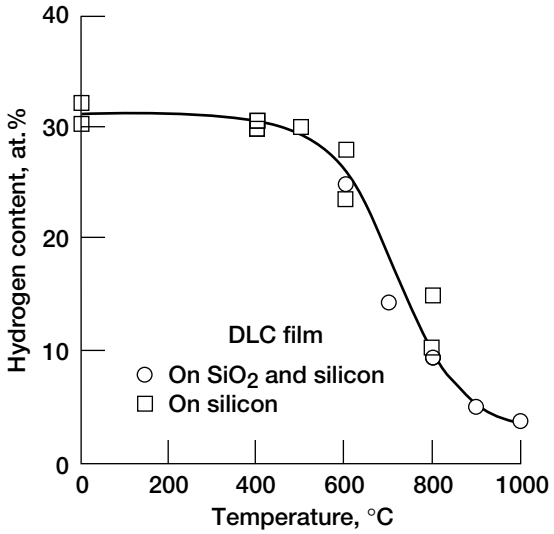

Figure 4.47.—Hydrogen content as function of rapid thermal annealing temperature for DLC films.

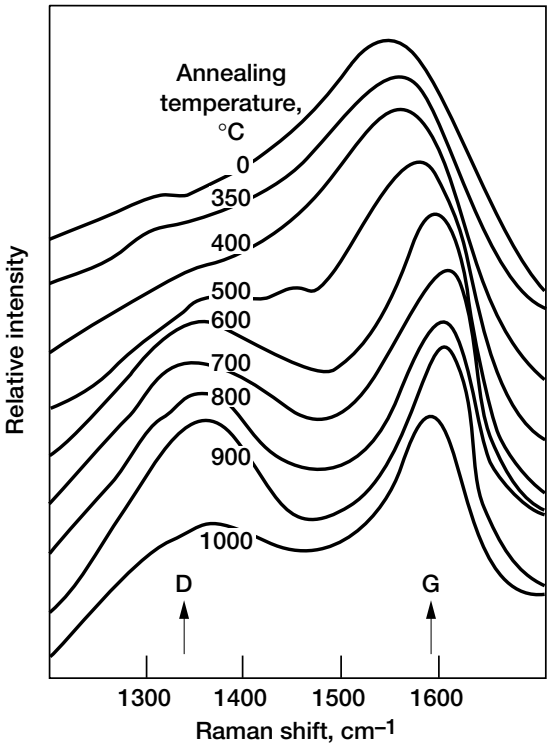

Figure 4.48.—Raman spectra from radio-frequency-plasma-deposited and rapid thermally annealed DLC films.

Figure 4.48 reveals that at 350 and 400 °C the Raman spectra of the as-radiofrequency-plasma-deposited DLC film and the rapid thermally annealed DLC films are quite similar. No phase change in the films was observed for annealing temperatures below 400 °C, consistent with Rutherford backscattering (RBS) and hydrogen forward-scattering (proton recoil detection) data. However, at 500 to 1000 °C the Raman spectra for the annealed DLC films were significantly different from the as-deposited DLC spectrum. As the rapid thermal annealing temperature increased, the full width at half-maximum (FWHM) of the "G" peak narrowed, and the peak shifted toward the graphitic peak at 1590 cm^{-1}, indicating a transition from less tetragonal bonding to more trigonal bonding. At the same time the intensity and FWHM of the "D" peak at 1350 cm^{-1} increased. The Raman spectra of the as-deposited DLC films heated above 400 °C show the appearance of the "D" peak at 1350 cm^{-1}, which is characteristic of disordered graphite with crystalline size less than 20 nm (200 Å) [4.49].

Experiments were performed in humid air (relative humidity (RH), ~40%) and in dry nitrogen (RH, <1%) with a 1.6-mm-radius Si_3N_4 pin contacting an as-deposited DLC film. Figure 4.49 presents the coefficients of friction obtained as a function of the number of repeated passes in reciprocating sliding. Much higher coefficients of friction were measured in humid air (above 0.15) than in dry nitrogen (~0.01). In the presence of moisture the coefficient of friction remained constant with increasing number of passes. This relatively higher, constant friction was the result of tribochemical interactions between the Si_3N_4 pin and moisture at the sliding interface [4.50–4.52]. The tribochemical interactions produced reaction products, such as SiO_2, at the sliding interface. These reaction products maintained the relatively higher constant friction in this case.

In dry nitrogen the initial coefficients of friction obtained were relatively high (0.12 to 0.15 in Fig. 4.49) due to adsorbed contaminants, primarily moisture, at the sliding interface. As sliding progressed, the coefficient of friction decreased to near 0.01 after approximately 2000 passes. This decrease in friction suggests that some contaminants, such as SiO_2 and moisture, were removed from the sliding surface of the Si_3N_4 pin during repeated passes in dry nitrogen.

The rapid thermally annealed DLC films exhibited similar friction behaviors as the as-deposited DLC film (see Fig. 4.49) in their respective environments. Figure 4.50 summarizes the equilibrium coefficients of friction for the as-deposited and rapid thermally annealed DLC films sliding against Si_3N_4 pins. These

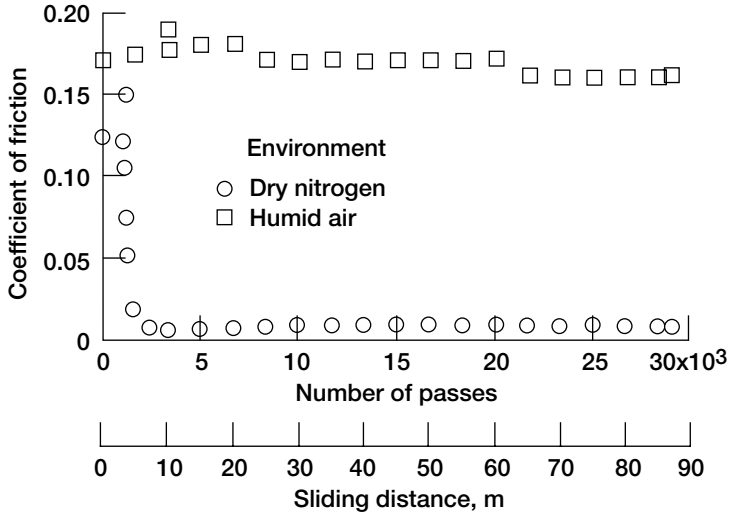

Figure 4.49.—Average coefficient of friction as function of number of passes for Si_3N_4 pin (1.6 mm in radius) in sliding contact with as-deposited DLC films in humid air and dry nitrogen at room temperature.

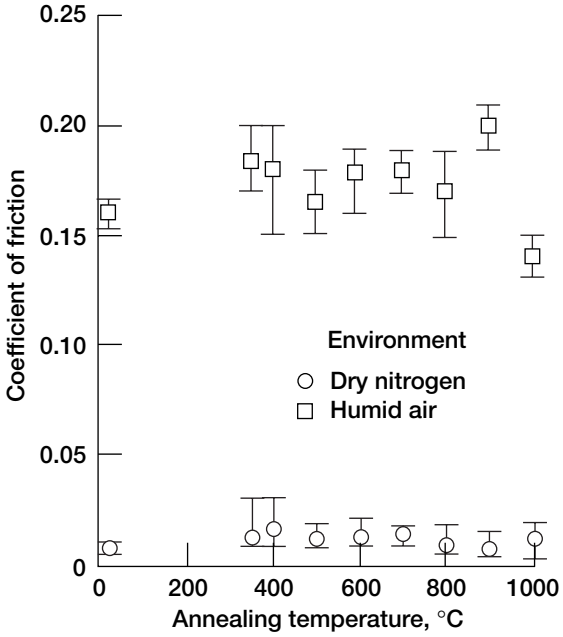

Figure 4.50.—Coefficients of friction in equilibrium state for as-deposited and rapid thermally annealed DLC films in sliding contact with Si_3N_4 pin in humid air and dry nitrogen at room temperature.

data indicate that annealing temperature had almost no effect on the equilibrium coefficients of friction in their respective environments.

Figure 4.51 presents the average wear rates of as-deposited and rapid thermally annealed DLC films contacting Si_3N_4 pins in humid air and dry nitrogen at room temperature. The effect of rapid thermal annealing on the wear rate in humid air and dry nitrogen was moderate except at annealing temperatures between 600 and 800 °C. The wear rates for the DLC films annealed between 600 and 800 °C drastically increased in humid air. As shown in Fig. 4.47 the hydrogen concentration of DLC films drastically decreased with increasing annealing temperature in this temperature range. The rapid evolution of hydrogen concentration in DLC films during annealing can be attributed to the creation of micropores and the roughing of the DLC surfaces. The high wear rates in humid air for DLC films annealed at 600 to 800 °C may be due to the high friction in humid air and the transformation of the DLC structure.

Although the rapid thermal annealing of DLC films does not affect their friction properties in humid air and dry nitrogen, thermal annealing significantly affects their friction properties in vacuum. For example, Fig. 4.52 shows an abrupt

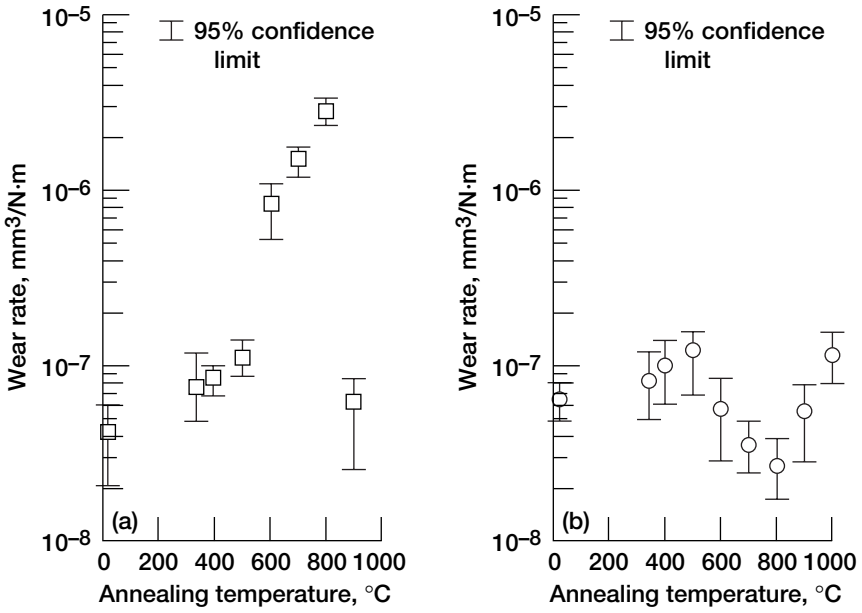

Figure 4.51.—Wear rates for as-deposited and rapid thermally annealed DLC films in sliding contact with Si_3N_4 pin (a) in humid air and (b) in dry nitrogen.

increase in coefficient of friction for DLC films annealed at temperatures between 500 and 600 °C in vacuum. In this investigation in situ single-pass sliding friction experiments were conducted in an ultrahigh vacuum (10^{-7} Pa) with plasma-deposited DLC (amorphous hydrogenated carbon, a-C:H) films on an Si_3N_4 flat in contact with an ion-sputter-cleaned, hemispherical Si_3N_4 pin (1.6 mm in radius). Loads were to 1.7 N (average Hertzian contact pressure, 1.5 GPa), and sliding velocity was 3 mm/min at temperatures to 700 °C. For the plasma-deposited DLC (a-C:H) films the coefficient of friction remained low to 500 °C and rapidly increased at 600 °C and above, remaining high from 600 to 700 °C. The mechanisms involved in this rapid increase in friction at 600 to 700 °C should be related to the two-step process—namely, carbonization and polymerization [4.53]. The carbonization stage includes loss of volatile matter, identified with hydrogen loss in this case [4.54]. This stage generally occurs in DLC films between 500 and 600 °C. The polymerization stage includes the formation of graphitic crystallites or sheets. The two-stage pyrolysis process of carbonization and polymerization occurs simultaneously in DLC films such as a-C:H. Under such conditions the sliding action produces failure in the film and at the interfacial adhesive bonds between the film and the substrate and causes film breakthrough in the contact area.

When the DLC film was ruptured, fresh surfaces of the Si_3N_4 couples came into direct contact, and the coefficient of friction rapidly increased to 0.7, almost the

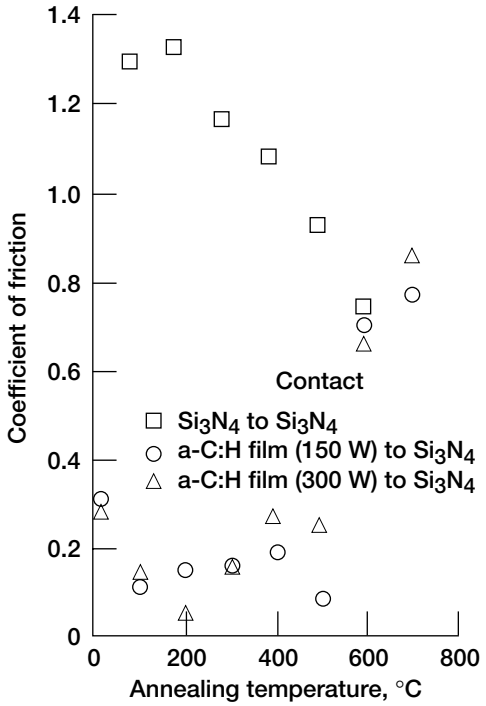

Figure 4.52.—Coefficients of friction for a-C:H-to-Si_3N_4 and Si_3N_4-to-Si_3N_4 contacts in vacuum.

same as that (0.75) for a bare Si_3N_4 flat in contact with a clean Si_3N_4 pin in ultrahigh vacuum, as shown in Fig. 4.52.

4.4.3 Silicon Nitride Coatings

Like DLC (amorphous hydrogenated carbon, a-C:H) films, amorphous hydrogenated silicon nitride (a-SiN_x:H) thin films transform at high temperatures (say above 500 °C). In as-deposited Si_3N_4 films hydrogen largely passivates nitrogen dangling bonds [4.55]. The hydrogen-nitrogen bonds can dissociate by high-temperature postdeposition heating or annealing, leaving behind charged nitrogen sites. As a matter of course, temperature could significantly influence the adhesion, friction, and wear of the Si_3N_4 films.

Adhesion and sliding friction experiments were conducted with Si_3N_4 films in contact with a hemispherical, monolithic, hot-pressed, polycrystalline, magnesia-doped Si_3N_4 pin at temperatures to 700 °C in vacuum [4.56]. Thin films (80 nm thick) containing Si_3N_4 were deposited by low- and high-frequency plasmas (30 kHz and 13.56 MHz) on silicon, GaAs, and InP substrates by using silane (SiH_4), ammonia (NH_3), and nitrogen gases in a parallel-plate plasma reactor.

Silicon nitride films.—AES analyses provided complete elemental depth profiles for the Si_3N_4 films on GaAs as a function of sputtering time. Figure 4.53 presents typical examples. The Si/N ratio was higher for the films deposited at 13.56 MHz than for those deposited at 30 kHz. XPS analyses (Table 4.5) also showed that Si/N ratios were much higher for the films deposited at 13.56 MHz and thus supported the AES data.

Table 4.6 gives film thicknesses determined with a rotating ellipsometer. The error margins are the 90% confidence limits. The results were obtained by using a model that assumed a single film on a substrate. The small error margins show that this model is an excellent description of the sample.

Figure 4.54 presents representative results for the refractive index η and the absorption coefficient α (where $\alpha = 4\pi K/\lambda$, K is the extinction coefficient, and λ is the wavelength) for two Si_3N_4 films on GaAs. The refractive index for the films deposited at 13.56 MHz was higher than that of pure amorphous Si_3N_4 [4.57], indicating that a small, but not insignificant, amount of amorphous silicon with its higher refractive index was present. In addition, pure Si_3N_4 does not absorb at all above 300 nm, whereas amorphous silicon does show absorption in the wavelength range used here. This fact and the results shown in Fig. 4.54(b), indicating

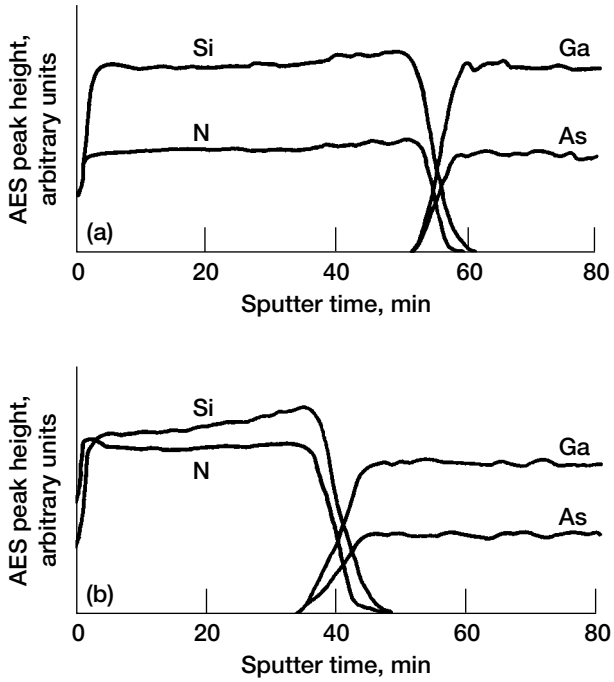

Figure 4.53.—AES depth profiles for Si_3N_4 films plasma deposited on GaAs (a) at high frequency (13.56 MHz) and (b) at low frequency (30 kHz).

TABLE 4.5.—Si/N RATIO IN Si_3N_4 FILMS

Substrate	Plasma deposition frequency	
	30 kHz	13.56 MHz
	Si/N ratio	
Si	1.1	1.4
GaAs	1.2	1.4
InP	1.1	1.7

TABLE 4.6.—FILM THICKNESS OF Si_3N_4 FILMS

Substrate	Plasma deposition frequency	
	30 kHz	13.56 MHz
	Film thickness, nm	
Si	77.1±0.2	85.6±0.2
GaAs	77.0±0.1	88.6±0.7
InP	76.1±0.1	76.6±0.1

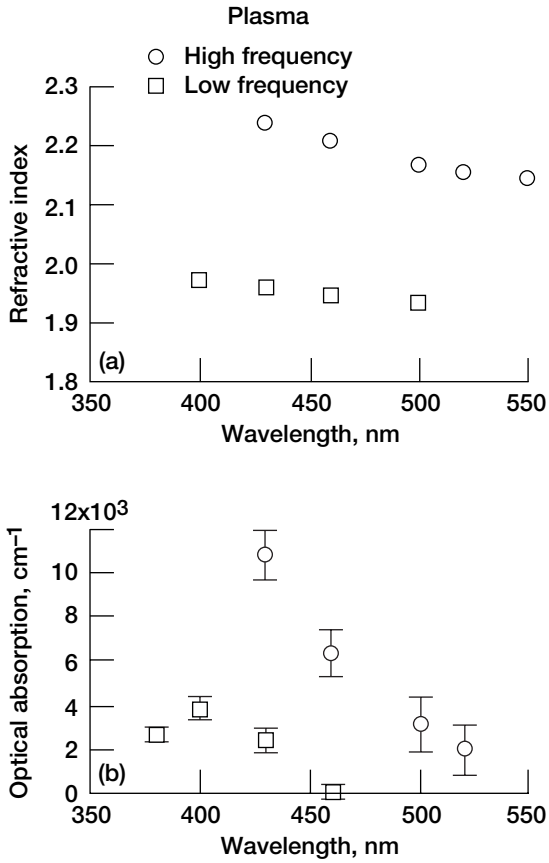

Figure 4.54.—Refractive index (a) and optical absorption (b) as function of wavelength for Si_3N_4 films plasma deposited on GaAs.

absorption in the films deposited at 13.56 MHz, reinforced the conclusion that amorphous silicon was present in these films.

The films deposited at 30 kHz had lower refractive indexes than pure Si_3N_4 and almost vanishing absorption. Therefore, these films contained either a small number of voids or a small amount of oxygen and a negligibly small amount of amorphous silicon. (Oxygen usually exists in the form of silicon oxynitride.)

Measurements of Si_3N_4 films on silicon and InP were similar to those obtained on GaAs. Thus, the difference in the properties of high- and low-frequency deposition is due only to the plasma, since there is no indication of substrate interaction.

Adhesion.—Adhesion experiments were conducted with plasma-deposited Si_3N_4 films in contact with monolithic, magnesia-doped Si_3N_4 at temperatures to 700 °C in ultrahigh vacuum. The adhesive strength is again defined as the force necessary to pull the surfaces apart. The monolithic Si_3N_4 pins were sputter cleaned with argon ions before the adhesion experiments. The plasma-deposited Si_3N_4 films were in the as-received state after they had been baked out in the vacuum system. At room temperature adsorbates from the environment were present on the plasma-deposited Si_3N_4 films. The results indicated no significant change in the pull-off force with respect to load over the load range 1 to 6 mN. The data, however, clearly suggest that adhesion depends on the temperature and the plasma deposition frequency.

Figure 4.55 presents the average pull-off forces for as-received Si_3N_4 films deposited by high- and low-frequency plasmas as a function of temperature. Although the pull-off force (adhesion) for the high-frequency films increased slightly from 0 to 400 °C, it generally remained low at these temperatures (Fig. 4.55(a)). The pull-off force increased significantly at 500 °C and remained high between 500 and 700 °C. Extremely strong adhesive bonding can take place at the contacting interface at temperatures in this range. However, the adsorbed carbon contaminant (determined by XPS) decreased rapidly with increasing temperature to 400 °C. Above 400 °C it had disappeared from the surface of the Si_3N_4 film. The rapid increase in adhesion at 500 to 700 °C correlated with this contaminant removal, resulting in a strong surface chemical reaction between the monolithic Si_3N_4 and the plasma-deposited Si_3N_4 film. In contrast, the low adhesion below 400 °C correlated with the presence of adsorbates. Also, the increase in adhesion at 500 °C correlated with the dissociation of the hydrogen-nitrogen bonds in the Si_3N_4 films. The hydrogen-nitrogen bond density does decrease during high-temperature heating [4.55].

For the Si_3N_4 films deposited by low-frequency plasma (30 kHz), the pull-off force increased with increasing temperature (Fig. 4.55(b)). When compared with the results of Fig. 4.55(a), however, the pull-off forces were generally lower in the high-temperature range (500 to 700 °C).

Friction and wear.—Figure 4.56 presents the coefficients of friction for Si_3N_4 films deposited by high-frequency plasma as a function of sliding temperature. The static friction characteristics (Fig. 4.56(a)) are the same as the adhesion characteristics (Fig. 4.55(a)). The coefficient of static friction increased slightly to

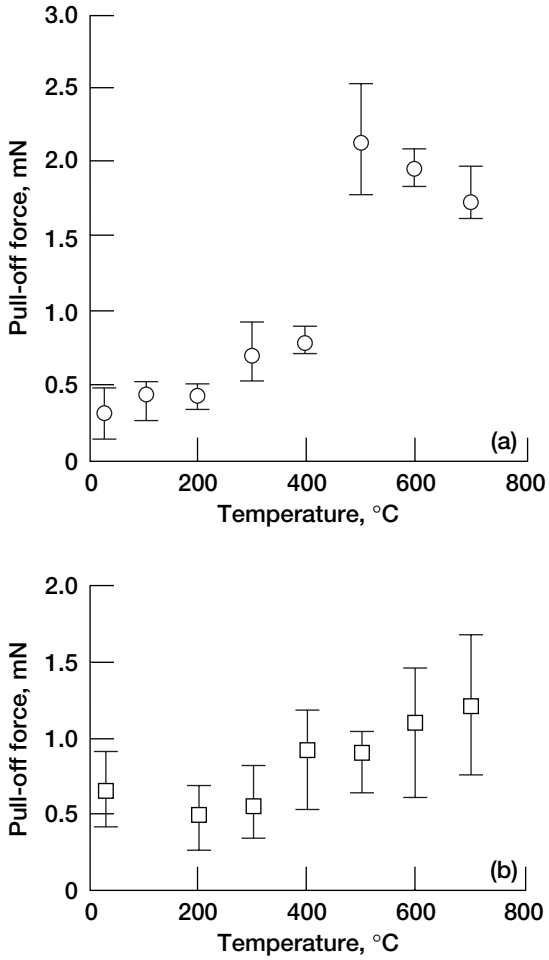

Figure 4.55.—Pull-off force (adhesion) as function of temperature for (a) high-frequency (13.56 MHz) and (b) low-frequency (30 kHz) plasma-deposited Si_3N_4 films in sliding contact with hemispherical monolithic Si_3N_4 pins in vacuum.

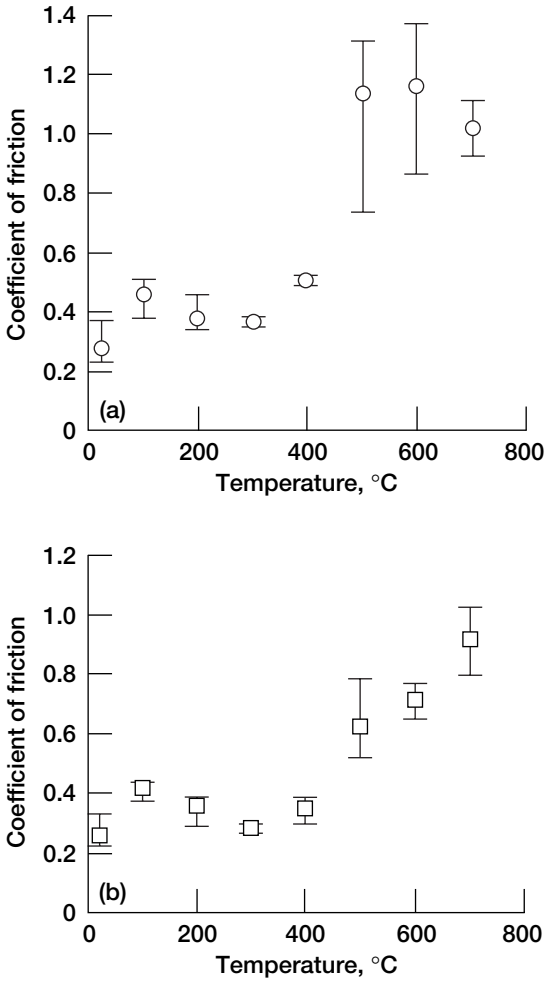

Figure 4.56.—Coefficient of friction as function of temperature for high-frequency-plasma-deposited Si_3N_4 films in sliding contact with hemispherical monolithic Si_3N_4 pins in vacuum. (a) Static friction. (b) Dynamic friction.

400 °C and rapidly above 500 °C, remaining high in the range 500 to 700 °C. The trend for the coefficient of dynamic friction (Fig. 4.56(b)) is also quite similar to that for adhesion. When compared with static friction, the coefficient of dynamic friction was generally lower below 700 °C.

Figure 4.57 shows the coefficients of friction for Si_3N_4 films deposited by low-frequency plasma as a function of sliding temperature. The static friction characteristics (Fig. 4.57(a)) are similar to the adhesion characteristics (Fig. 4.55(a)). The coefficient of static friction increased slightly to 500 °C and quite rapidly after 500 °C, remaining high between 600 and 700 °C. The trend for the coefficient of

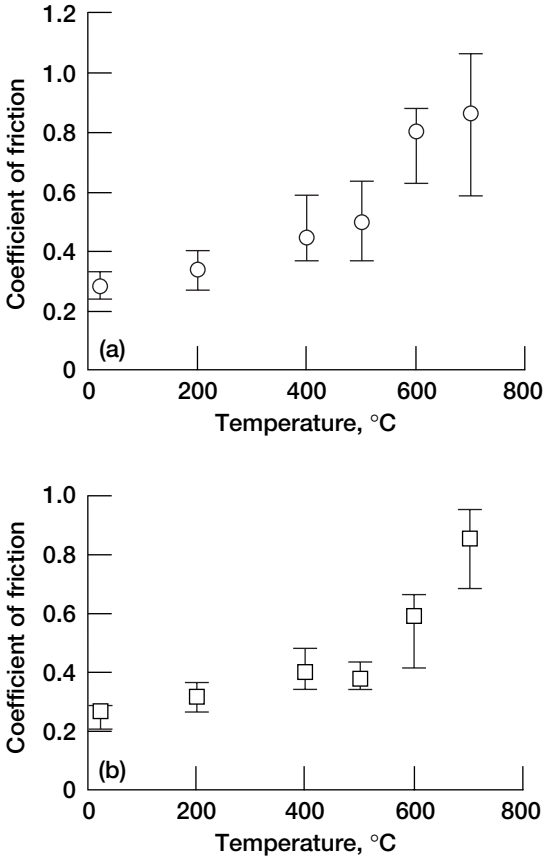

Figure 4.57.—Coefficient of friction as function of temperature for low-frequency-plasma-deposited Si_3N_4 films in sliding contact with hemispherical monolithic Si_3N_4 pins in vacuum. (a) Static friction. (b) Dynamic friction.

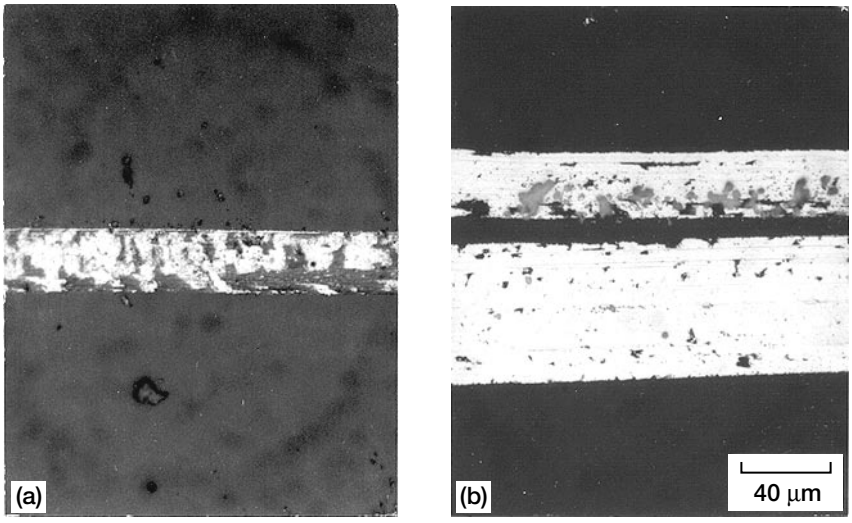

Figure 4.58.—Optical photomicrographs of wear tracks generated by hemispherical monolithic Si_3N_4 pins sliding at high temperatures in vacuum on high-frequency-plasma-deposited (13.56 MHz) Si_3N_4 film surfaces. (a) At 500 °C. (b) At 700 °C.

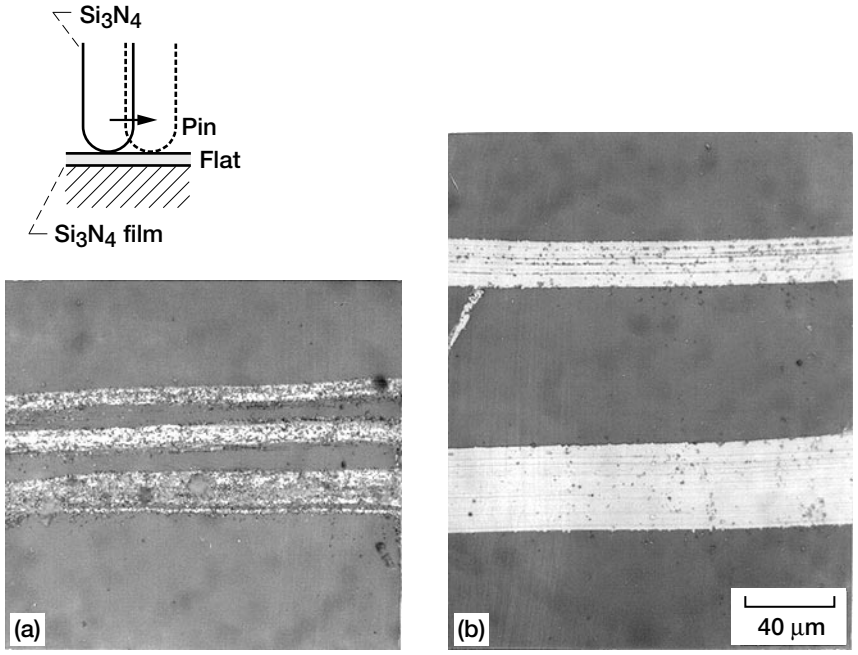

Figure 4.59.—Optical photomicrographs of wear tracks generated by hemispherical monolithic Si_3N_4 pins sliding at high temperatures in vacuum on low-frequency-plasma-deposited (30 kHz) Si_3N_4 film surfaces. (a) At 500 °C. (b) At 700 °C.

dynamic friction (Fig. 4.57(b)) was also similar to that for adhesion. When compared with static friction, the coefficient of dynamic friction was generally lower below 700 °C.

When the sliding temperature was increased to 500 to 700 °C, the sliding action produced failure in the films and at the interfacial adhesive bonds between the film and the substrate and caused film breakthrough in the contact area (Figs. 4.58 and 4.59). Also, wear debris particles of Si_3N_4 film were observed. Thus, the increase in friction at higher loads was caused by the gross failure of the Si_3N_4 film. A large amount of frictional energy was dissipated as the film failed during sliding.

Thus, as anticipated, there was a significant temperature influence on the adhesion, friction, and wear of Si_3N_4 films. The changes in tribological properties at high temperatures are primarily related to the dissociation of hydrogen-nitrogen bonds.

The adhesion behavior of the plasma-deposited Si_3N_4 films at temperatures to 700 °C was similar to that of the coefficient of friction. Although adhesion and friction remained low to 400 °C and the temperature effect was small, they increased greatly above 500 to 600 °C.

Source wear of the Si_3N_4 film occurred in the contact area at high temperatures. The wear correlated with the increase in adhesion and friction for the low- and high-frequency-plasma-deposited films above 600 and 500 °C, respectively.

4.5 Concluding Remarks

Studies are described characterizing the contributions of surface contamination and chemical changes to tribology. Examples are given from in situ adhesion and friction experiments in which surface analyses have contributed significantly to the elucidation of phenomena, reactions, and processes in tribology.

Surface contaminant films formed by the interaction of a surface with the environment affect the adhesion and friction behavior of surfaces. An adsorbed carbon contaminant on a ceramic surface can greatly reduce adhesion and, accordingly, friction.

With ceramics in contact with themselves or metals, nitrogen and oxygen as surface contaminant films generally decrease interfacial bond strengths and accordingly friction, while some defined exposure of these materials to oxygen increases both adhesion and friction.

Contaminants can diffuse from the bulk of materials to the surface upon heating. The formation and segregation of contaminants such as oxides are responsible for adhesion and friction behavior.

Heating material to a high temperature can result in selective thermal evaporation. For example, with silicon carbide, silicon volatilizes and leaves behind a graphitic film that reduces adhesion and friction.

With hydrogenated carbon coatings and hydrogenated silicon nitride coatings, hydrogen volatilizes and leaves behind a weakly bonded coating.

References

4.1 D.H. Buckley, *Surface Effects in Adhesion, Friction, Wear and Lubrication, Tribology Series*, Elsevier Scientific Publishing Co., New York, Vol. 5, 1981.

4.2 D. Tabor, Status and direction of tribology as a science in the 80's—understanding and prediction, *New Directions in Lubrication, Materials, Wear, and Surface Interactions* (W.R. Loomis, ed.), Noyes Publications, Park Ridge, NJ, Vol. 1, 1984, pp. 1–17. (Also NASA CP–2300.)

4.3 K. Miyoshi, Uses of Auger and x-ray photoelectron spectroscopy in the study of adhesion and friction, *Advances in Engineering Tribology* (Y.-W. Chung and H.S. Cheng, eds.), STLE SP–31, Society of Tribologists and Lubrication Engineers, Park Ridge, IL, 1991, pp. 3–12.

4.4 K. Miyoshi and Y.W. Chung, *Surface Diagnostics in Tribology*, World Scientific Publishing Co., Inc., River Edge, NJ, 1993.

4.5 L. Pauling, A resonating-valence-bond theory of metals and intermetallic compounds, *Proc. R. Soc. London A196*: 343–362 (1949).

4.6 K. Miyoshi, J.J. Pouch, and S.A. Alterovitz, Plasma-deposited amorphous hydrogenated carbon films and their tribological properties, *Mater. Sci. Forum 52–53*: 645–656 (1989).

4.7 J.J. Pouch, S.A. Alterovitz, K. Miyoshi, and J.D. Warner, Boron nitride: composition, optical properties, and mechanical behavior, *Materials Modification and Growth Using Ion Beams* (U.J. Gibson, A.E. White, and P.P. Pronko, eds.), Materials Research Society, Pittsburgh, PA, Vol. 93, 1987, pp. 323–328.

4.8 F.T. Barwell, Metallic wear, *CRC Handbook of Lubrication* (E.R. Booser, ed.), CRC Press, Inc., Boca Raton, Florida, Vol. 2, 1984, pp. 163–184.

4.9 E. Rabinowicz, Wear coefficients, *CRC Handbook of Lubrication* (E.R. Booser, ed.), CRC Press, Inc., Boca Raton, Florida, Vol. 2, 1984, pp. 201–208.

4.10 K. Miyoshi et al., Friction and wear of plasma-deposited diamond films, *J. Appl. Phys. 74, 7*: 4446–4454 (1993).

4.11 I. Langmuir, The constitution and fundamental properties of solids and liquids, Part I–Solids, *J. Am. Chem. Soc. 38, 11*: 2221–2295 (1916).

4.12 J.E. Lennard-Jones, Processes of adsorption and diffusion on solid surfaces, *Trans. Faraday Soc. 28*: 333–359 (1932).

4.13 H.S. Taylor, The activation energy of adsorption processes, *J. Am. Chem. Soc. 53, 2*: 578–597 (1931).

4.14 J.K. Roberts, The adsorption of hydrogen on tungsten, *Proc. R. Soc. London A152, 876*: 445–477 (1935).

4.15 C.W. Oatley, The adsorption of oxygen and hydrogen on platinum and the removal of these gases by positive ion bombardment, *Proc. Phys. Soc. London 51, 2*: 318–328 (1939).

4.16 J.A. Dillon, Jr., The Interaction of oxygen with silicon carbide surfaces, *Silicon Carbide, a High Temperature Semiconductor* (J.R. O'Connor, and J. Smitems, eds.), Pergamon Press, Oxford, 1960, pp. 235–240.

4.17 J.S. Johannessen, W.E. Spicer, and Y.E. Strausser, An Auger analysis of the SiO_2-Si interface, *J. Appl. Phys. 47, 7*: 3028–3037 (1976).

4.18 K. Miyoshi and D.H. Buckley, Effect of oxygen and nitrogen interactions on friction of single-crystal silicon carbide, NASA TP–1265 (1978).

4.19 L. Brewer, L.A. Bromley, P.W. Gilles, and N.L. Lofgren, Thermodynamic and physical properties of nitrides, carbides, sulfides, silicides, and phosphides, *The Chemistry and Metallurgy of Miscellaneous Materials: Thermodynamics* (L.L. Quill, ed.), McGraw-Hill, New York, 1950, pp. 40–59.

4.20 F.D. Rossin et al., Selected values of chemical thermodynamic properties, *Circular of the National Bureau of Standards 500*, U.S. Government Printing Office, Washington, DC, 1952.

4.21 K. Miyoshi and D.H. Buckley, X-ray photoelectron spectroscopy and friction studies of nickel-zinc and manganese-zinc ferrites in contact with metals, NASA TP–2163 (1983).
4.22 K. Miyoshi, C. Maeda, and R. Masuo, Development of a torsion balance for adhesion measurements, *IMEKO XI: Instrumentation for the 21st Century*: Proceedings of the 11th Triennial World Congress of the International Measurement Confederation (IMEKO), Instrument Society of America, Triangle Park, NC, 1988, pp. 233–248.
4.23 D.D. Eley, *Adhesion*, Oxford University Press, London, 1961.
4.24 F.P. Bowden and D. Tabor, Action of extreme pressure lubricants, *The Friction and Lubrication of Solids—Part XI*, Clarendon Press, Oxford, 1958, pp. 228–314.
4.25 K. Miyoshi and D.H. Buckley, Effects of water vapor on friction and deformation of polymeric magnetic media in contact with a ceramic oxide, *Tribology and Mechanics of Magnetic Storage Systems* (B. Bushan et al., eds.), STLE SP–16, Society of Tribologists and Lubrication Engineers, Park Ridge, IL, 1984, pp. 27–34.
4.26 K. Miyoshi and D.H. Buckley, Friction and deformation behavior of single-crystal silicon carbide, NASA TP–1053 (1977).
4.27 F.P. Bowden and D. Tabor, *The Friction and Lubrication of Solids—Part II*, Clarendon Press, Oxford, 1964.
4.28 K. Miyoshi, D.H. Buckley, and B. Bhushan, Friction and morphology of magnetic tapes in sliding contact with nickel-zinc ferrite, NASA TP–2267 (1984).
4.29 R.L. Bradshaw and B. Bhushan, Friction in magnetic tapes III: role of chemical properties, *ASLE Trans. 27, 3*: 207–219 (1984).
4.30 V.D. Scott and H. Wilman, Surface reorientation caused on metals by abrasion—its nature, origin, and relation to friction and wear, *Proc. Roy. Soc. London A 247, 1250*: 353–368 (1958).
4.31 J. Goddard, H.J. Harker, and H. Wilman, The surface reorientation caused by unidirectional abrasion on face-centered cubic metals, *Proc. Phys. Soc. London 80:* 771–782 (1962).
4.32 D.H. Buckley, Recrystallization and preferred orientation in single-crystal and polycrystalline copper in friction studies, NASA TN D–3794 (1967).
4.33 K. Miyoshi and D.H. Buckley, Sliding-induced crystallization of metallic glass, NASA TP–2140 (1983).
4.34 K. Miyoshi and D.H. Buckley, Surface chemistry, microstructure, and friction properties of some ferrous-base metallic glasses at temperatures to 750 °C, NASA TP–2006 (1982).
4.35 K. Miyoshi and D.H. Buckley, Friction and wear of some ferrous-base metallic glasses, *ASLE Trans. 27, 4*: 295–304 (1984). (Also NASA TM–83067.)
4.36 K. Miyoshi and D.H. Buckley, Friction and surface chemistry of some ferrous-base metallic glasses, NASA TP–1991 (1982).
4.37 D.V. Badami, X-ray studies of graphite formed by decomposing silicon carbide, *Carbon 3, 1*: 53–57 (1965).
4.38 K. Miyoshi and D.H. Buckley, Surface chemistry and wear behavior of single-crystal silicon carbide sliding against iron at temperatures to 1500 °C in vacuum, NASA TP–1947 (1982).
4.39 K. Miyoshi, D.H. Buckley, and M. Srinivasan, Tribological properties of sintered polycrystalline and single-crystal silicon carbide, *Am. Ceram. Soc. Bull. 62, 4*: 494–500 (1983).
4.40 R.C. Weast, ed., *CRC Handbook of Chemistry and Physics: A Ready Reference Book of Chemical and Physical Data*, 68th ed., CRC Press Inc., Boca Raton, FL, 1987.
4.41 D.H. Buckley and W.A. Brainard, Friction and wear of metals in contact with pyrolytic graphite, *Carbon 13, 6*: 501–508 (1975).
4.42 K. Miyoshi and D.H. Buckley, Considerations in friction and wear, *New Directions in Lubrication, Materials, Wear, and Surface Interactions* (W.R. Loomis, ed.), Noyes Publications, Park Ridge, NJ, Vol. I, 1984, pp. 282–319. (Also NASA CP–2300.)
4.43 F. Meyer and G.J. Loyen, Ellipsometry applied to surface problems—optical layer thickness measurement, *Acta Electron 18*: 33–38 (1975).
4.44 A.J. Van Bommel, J.E. Crombeen, and A. Van Tooren, LEED and Auger electron observations of the SiC (0001) surface, *Surf. Sci. 48, 2*: 463–472 (1975).

4.45 H.O. Pierson, Structure and properties of diamond and diamond polytypes, *Handbook of Carbon, Graphite, Diamond, and Fullerenes*, Noyes Publications, Park Ridge, NJ, 1993, pp. 244–277.
4.46 R.L.C. Wu, K. Miyoshi, R. Vuppuladhadium, and H.E. Jackson, Physical and tribological properties of rapid thermal annealed diamond-like carbon films, *Surf. Coat. Tech., 54/55*: 576–580 (1992).
4.47 D.I. Jones and A.D. Stewart, Properties of hydrogenated amorphous carbon films and the effects of doping, *Phil. Mag. B 46*: 423–434 (1982).
4.48 B. Dischler, A. Bubenzer, and P. Koidl, Bonding in hydrogenated hard carbon studied by optical spectroscopy, *Solid State Commun. 48, 2*: 105–108 (1983).
4.49 R.O. Dillon, J.A. Woollam, and V. Katzanant, Use of Raman scattering to investigate disorder and crystallite formation in as-deposited and annealed carbon films, *Phys. Rev. B 29*: 3482–3489 (1984).
4.50 T. Sugita, K. Ueda, and Y. Kanemura, Material removal mechanism of silicon nitride during rubbing in water, *Wear 97*: 1–8 (1984).
4.51 T.E. Fischer and H. Tomizawa, Interaction of tribochemistry and microfracture in the friction and wear of silicon nitride, *Wear of Materials 1985* (K.C. Ludema, ed.), American Society of Mechanical Engineers, New York, 1985, pp. 22–32.
4.52 H. Ishigaki and K. Miyoshi, Tribological properties of ceramics, *Proceedings of the 6th International Conference on Production Engineering, Osaka 1987*, Japan Society of Precision Engineering, Tokyo, 1987, pp. 661–666.
4.53 J. Robertson, Amorpous carbon, *Adv. Phys. 35, 4*: 317–374 (1986).
4.54 J.C. Angus, P. Koidl, and S. Domitz, Carbon thin films, *Plasma-Deposited Thin Films* (J. Mort and F. Jansen, eds.), CRC Press, Inc., Boca Raton, FL, 1986, pp. 89–127.
4.55 W.L. Warren et al., Creation and properties of nitrogen dangling bond defects in silicon nitride thin films, *J. Electrochem. Soc. 143, 11*: 3685–3691 (1996).
4.56 K. Miyoshi et al., Adhesion, friction, and wear of plasma-deposited thin silicon nitride films at temperatures to 700 °C, *Wear 133*: 107–123 (1989).
4.57 E.D. Palik, *Handbook of Optical Constants of Solids*, Academic Press, Orlando, FL, 1985.

REPORT DOCUMENTATION PAGE

Form Approved
OMB No. 0704-0188

1. AGENCY USE ONLY (*Leave blank*)	2. REPORT DATE	3. REPORT TYPE AND DATES COVERED
	July 1998	Technical Memorandum

4. TITLE AND SUBTITLE

Solid Lubrication Fundamentals and Applications
Properties of Contaminated Surfaces: Adhesion, Friction, and Wear

5. FUNDING NUMBERS

WU–505–63–5A

6. AUTHOR(S)

Kazuhisa Miyoshi

7. PERFORMING ORGANIZATION NAME(S) AND ADDRESS(ES)

National Aeronautics and Space Administration
Lewis Research Center
Cleveland, Ohio 44135–3191

8. PERFORMING ORGANIZATION REPORT NUMBER

E–9863–4

9. SPONSORING/MONITORING AGENCY NAME(S) AND ADDRESS(ES)

National Aeronautics and Space Administration
Washington, DC 20546–0001

10. SPONSORING/MONITORING AGENCY REPORT NUMBER

NASA TM—1998-107249
CH4

11. SUPPLEMENTARY NOTES

Responsible person, Kazuhisa Miyoshi, organization code 5140, (216) 433–6078.

12a. DISTRIBUTION/AVAILABILITY STATEMENT

Unclassified - Unlimited
Subject Category: 27 Distribution: Nonstandard

This publication is available from the NASA Center for AeroSpace Information, (301) 621–0390.

12b. DISTRIBUTION CODE

13. ABSTRACT ***(Maximum 200 words)***

This chapter presents the adhesion, friction, and wear behavior of smooth but contaminated surfaces of solid-solid couples, such as metal-ceramic couples. Effects of surface contamination formed by the interaction of a surface with the environment, surface contamination obtained with diffusion of bulk compounds, and surface chemical changes resulting from selective thermal evaporation on the adhesion, friction, and wear behaviors of solid-solid couples are described. The primary emphasis is to relate adhesion, friction, and wear to reactions at the interface and to the composition of the interface. Also, the friction mechanisms of contaminated, smooth surfaces are stated in various parts of this chapter.

14. SUBJECT TERMS

Solid lubrication; Coatings; Tribology fundamentals; Applications

15. NUMBER OF PAGES

83

16. PRICE CODE

A05

17. SECURITY CLASSIFICATION OF REPORT	18. SECURITY CLASSIFICATION OF THIS PAGE	19. SECURITY CLASSIFICATION OF ABSTRACT	20. LIMITATION OF ABSTRACT
Unclassified	Unclassified	Unclassified	